A&A, 711, A198 (2026)
https://doi.org/10.1051/0004-6361/202659915

Astronomy & Astrophysics

The small transiting planet population revealed by ESPRESSO with extreme precision radial velocities

M. J. Hobson[1,⋆], B. Lavie[1], F. Bouchy[1], C. Lovis[1], F. Pepe[1], S. G. Sousa[2,3], H. M. Tabernero[4,5], S. E. van Terwisga[6], S. Oe[8,7], V. Adibekyan[2,3], C. Allende Prieto[9,10], Y. Alibert[11,12], S. C. C. Barros[2,3], A. Castro-González[1], S. Cristiani[13,14], V. D'Odorico[13], O. D. S. Demangeon[2], X. Dumusque[1], D. Ehrenreich[1], P. Figueira[15], R. Génova Santos[9], J. I. González Hernández[9,10], J. Lillo-Box[16], G. Lo Curto[17], C. J. A. P. Martins[18,2], P. Di Marcantonio[13], A. Mehner[17], G. Micela[19], P. Molaro[13], N. J. Nunes[20], E. Palle[9,10], R. Rebolo[9,10,21], J. Rodrigues[2,3,1], N. Santos[2,3], A. Sozzetti[22], S. Udry[1], A. Suárez Mascareño[9,10], and M.-R. Zapatero Osorio[16]

(Affiliations can be found after the references)

Received 17 March 2026 / Accepted 22 May 2026

ABSTRACT

Context. Small planets are extremely common in the Galaxy, including planets with masses and radii between those of Earth and Neptune. Characterising the mass of such planets requires ultra-precise radial velocities. The ESPRESSO spectrograph was designed and built for this purpose.

Aims. We present an overview of the ESPRESSO Guaranteed Time Observations transit follow-up sub-programme, which aimed to confirm and characterise small transiting planet candidates from the K2 and TESS space missions.

Methods. We analysed the global stellar and planetary properties of the sample of 65 planets in 30 systems characterised by this sub-programme. This includes six systems presented in this paper, for which we either obtain only the upper mass limits or provide updates to previously published parameters. We also placed this sample in the context of the overall population of precisely characterised small planets.

Results. After separating the population into insolation regimes, we find a tentative mass threshold at $\simeq 6\,M_\oplus$ for the rocky to volatile-rich composition transition in the medium-insolation regime, along with a population of likely stripped massive rocky planets in the high-insolation regime. Likewise, we find a correlation between planet mass and stellar metallicity, with more massive planets hosted by more metal-rich stars. We also explored the radius valley, finding that planets below the gap have a tighter mass distribution. We compared planetary masses with typical protoplanetary disk masses, drawing tentative conclusions about likely formation conditions. We also discuss the impact of our observing strategy on our results.

Conclusions. The ESPRESSO transit follow-up sub-programme has been highly productive in characterising a diverse population of small planets, which has enabled us to identify population-level features. Likewise, the lessons learned from this sub-programme will be valuable for PLATO follow-up planning.

Key words. techniques: polarimetric – techniques: radial velocities – planets and satellites: composition – planets and satellites: detection

1. Introduction

The most common planets in the Galaxy are super-Earths and sub-Neptunes (Mayor et al. 2011; Fressin et al. 2013). These planets, with masses and radii between those of Earth and Neptune, are intriguing since such planets are not found in the Solar System, raising questions about their likely compositions. Scaled-up Earths, scaled-down Neptunes, gas dwarfs, and water worlds have all been proposed as options (e.g. Valencia et al. 2007; Fortney et al. 2007; Rogers 2015; Zeng et al. 2019; Bean et al. 2021; Luo et al. 2024; Parc et al. 2024, and references therein). Likewise, they are among the most promising candidates for habitability (Heller & Armstrong 2014). However, due to their small sizes and low masses, they are also some of the hardest planets to detect and characterise, requiring highly precise instrumentation.

The shallow transits from small planets are difficult to capture with ground-based (and, thus, atmosphere-limited) facilities and, as a result, the technique is relatively inefficient for large blind surveys from the ground. Instead, they are primarily identified by space-based missions such as *Kepler*, K2, and TESS. *Kepler* (Borucki et al. 2010) was active from April 2009 to May 2013, observing the same sector of the northern sky for four years. While it identified thousands of transiting planet candidates, most orbit faint stars, making radial velocity (RV) follow-up difficult or impossible. Likewise, the Kepler field is inaccessible to southern RV facilities. *Kepler*'s successor mission, K2 (Howell et al. 2014), was active from June 2014 to October 2018, and observed 19 campaigns of around three months each along the ecliptic, covering a field of 115 square degrees in each campaign. Meanwhile, TESS (Ricker et al. 2015), which began operations in 2018 and is still observing today, observes 3200 square degree sectors for 27 days each, covering most of the sky in sequence. Both K2 and TESS observed brighter stars than

⋆ Corresponding author: melissa.hobson@unige.ch

the *Kepler* mission, and observed regions of the sky accessible to southern velocimetric facilities.

The premier southern extreme precision radial velocity (EPRV) facility is the Echelle SPectrograph for Rocky Exoplanets and Stable Spectroscopic Observations (ESPRESSO, Pepe et al. 2013, 2021) at ESO's Very Large Telescope (VLT), Paranal, Chile. ESPRESSO is a fibre-fed echelle spectrograph covering the 378.2–788.7 nm wavelength range, with a simultaneous reference fibre that can observe either the sky or a calibration lamp. It can observe with any of the four Unit Telescopes (UTs) of the VLT, reaching a resolving power of 140 000 (high-resolution mode) or 190 000 (ultra-high resolution mode). It can also observe with all four UTs together, with a resolving power of 70 000. Being designed for ultra-high RV precision, ESPRESSO is thus ideally suited to precisely determining the masses of low-mass planets. It has been shown to achieve an RV precision better than 25 cm s^{-1} during a single night (Pepe et al. 2021) and of 40 cm s^{-1} over 3.5 years (Figueira et al. 2025).

Since October 2018, the ESPRESSO consortium has been carrying out an ambitious programme of low-mass planet characterisation, through its Guaranteed Time Observations (GTO, Pepe et al. 2021). One of the major sub-programmes, known as Working Group 3 (WG3), is dedicated to the follow-up of candidate transiting small planets from TESS and K2. In this paper, we present an overview of the entire WG3 sub-programme. Section 2 describes the WG3 goals and observing strategy, and summarises the resulting discoveries. In Section 3, we analyse previously unpublished ESPRESSO datasets for six systems for which we either obtain only upper mass limits on the transiting planets or provide parameter updates and refinements to previously published planets using other facilities. We also provide stellar parameters for 15 stars for which less than 10 measurements were obtained with ESPRESSO and whose RVs we provide in this work, but do not analyse further. Section 4 explores the population of planets from the WG3 sub-programme, including all published and in prep planet detections. We also explore population-level features such as the radius valley, the mass-metallicity correlation, and the comparison of planet masses to typical disk masses, and discuss the impact of the observing strategy and stellar activity. Finally, we present our conclusions in Section 5.

2. Overview of the WG3 sub-programme

2.1. Goals and sample definition

The main goals of the ESPRESSO GTO WG3 sub-programme are:

1. the confirmation and detailed characterisation of small rocky transiting planet candidates;
2. the probing of the rocky-to-gaseous transition.

For the first goal, the sample was selected from K2 and TESS validated or vetted candidates with $R_p \lesssim 2\,R_\oplus$, orbiting bright stars ($V \lesssim 14.5$) and with no mass measurement available. For the second, Fulton et al. (2017) suggested that the insolation range of $50\,S_\oplus \lesssim S_p \lesssim 200\,S_\oplus$ was particularly interesting, as sub-Neptunes and rocky planets coexist there. The sample for this goal was thus constructed to include all the more massive companions to the rocky planet sample, plus other sub-Neptune and Neptune candidates with $R_p \lesssim 4\,R_\oplus$ within this insolation range.

Figure 1 shows the sample regions and the planets characterised by the WG3, together with the overall population of small planets, and the TESS and K2 candidates from

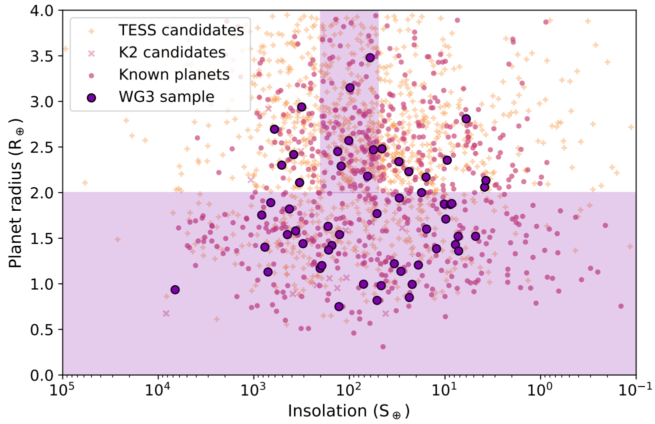

Fig. 1. WG3 sample region (purple shaded areas) and individual target planets (purple circles), together with the population of confirmed and validated small planets (pink circles) and TESS and K2 candidates (orange plusses and pink crosses, respectively). Target planets outside the sample regions are either part of multiplanetary systems with planets within the sample regions, or were initially thought to fall within them.

which our targets were drawn. Most of the WG3 planets outside the target regions are in multiplanetary systems with companions within them. The exceptions are π Men c (Damasso et al. 2020), TOI-283 c (Murgas et al. 2025), and BD+20954 b (this work), all of which were initially announced as having radii of $\sim 2\,R_\oplus$ and thus considered as falling within the sample region, but whose final radii are slightly above $2\,R_\oplus$.

2.2. Observations and results

The observations for the WG3 were carried out between September 2018 and March 2023, spanning four-and-a-half years. There was, however, a nine-month interruption in 2020, when the Paranal observatory was closed in response to the COVID-19 pandemic. The targets to be observed were drawn from candidates in our sample region, with additional considerations such as observability from Paranal, stellar brightness, or stellar activity level. Bright targets were particularly prioritised, as they require less observing time for equal RV precision and, thus, enable more systems to be followed. We did not observe the same targets over the entire duration, but dynamically updated the target list as new candidates were released by TESS. A total of 50 stars were observed, although 15 of these were dropped after a handful of observations for varied reasons, such as the fact that they were already intensively followed by other teams or the RV photon-noise uncertainties and/or level of stellar activity were too large for precise mass characterisation.

Individual WG3 targets were observed over time spans of 2 to 36 months, with the average baseline being of 16 months. We used the 1-UT, high resolution mode for all observations. The binning and readout mode, exposure time, and use of the calibration fibre were selected according to the target magnitude, as summarised in Table 1. Regarding observing strategy, we generally requested measurements every 2–4 nights depending on the orbital period of the planet candidate(s).

The WG3 sub-programme has been highly productive. From these observations, 54 planets around 23 stars have been (or will shortly be) published by the ESPRESSO GTO consortium. In Table 2 we list the planets, their main characteristics, and the reference WG3 publication. A further ten planets around six

Table 1. Observing strategy summary for the WG3 targets by target magnitude.

V magnitude	Binning and readout	Exposure time	Calibration fibre
Π Men C (V=5.7)	1 × 1, FAST	6 × 120 s	FP
V < 411	1 × 1, FAST	900 s	FP
11 < V < 12	2 × 1, SLOW	900 s	Sky
12 < V < 13	2 × 1, SLOW	1200 s	Sky
V > 13	2 × 1, SLOW	1800 s	Sky

stars are presented in this paper. For six of them we can provide only upper mass limits based on the existing data. The remaining four were previously published by other groups; we use the ESPRESSO RVs, together with the published data, to provide parameter updates. Combining the two groups, this comprises a final total of 65 planets in 30 systems. We note that some of these planets are non-transiting companions to transiting planets, that were revealed by the RV data. For these planets, we report the minimum mass.

2.3. Some remarkable individual systems

There are many noteworthy individual planets and planetary systems among the WG3 harvest. Here, we highlight a small selection. Considering the sample as a whole, the lowest-mass planet detected is TOI-175 b (Demangeon et al. 2021, also known as L 98-59 b), with less than half the mass of the Earth. This is not, however, the smallest RV signal detected, as the RV semi-amplitude is a combination of the stellar mass, planetary mass, and orbital period; that honour goes to TOI-174 d, e, and f (Barros et al. 2022), all at 29 – 30 cm s^{-1}. The densest planet of the sample is TOI-2322 c (Hobson et al. 2025), a remarkably massive super-Earth, while the least dense planet is TOI-178 g (Leleu et al. 2021), a mini-Neptune with a large gas fraction. Regarding density, we also highlight TOI-175 d (Demangeon et al. 2021) and TOI-244 b (Castro-González et al. 2023), two of the first low-density super-Earths to be discovered; and K2-38 b (Toledo-Padrón et al. 2020), with an extraordinarily dense, Mercury-like composition. While around half the planets have periods shorter than 10 days, there are a handful of transiting planets with periods longer than 35 days: BD+20594 b (this work), TOI-286 c (Hobson et al. 2024), TOI-713 c (Barros et al., in prep), and TOI-186 b (Dragomir et al. 2019, this work). Insolation-wise, the planets range from K2-157 b (Castro-González et al. 2025) at over 6000 times the Earth's insolation, to TOI-270 d (Van Eylen et al. 2021), the lowest insolation transiting planet in the sample at less than 4 $S_{\oplus}$; there are also non-transiting outer companions to transiting planets at insolations down to a tenth of the Earth's (TOI-1444 b, Damasso et al. 2020). The TOI-178 system (Leleu et al. 2021, 2024), comprised of six small planets in which all but the innermost are in a chain of Laplace resonances, has the largest number of planets out of the systems in the sample, closely followed by the TOI-174 system (Barros et al. 2022) with five planets.

3. Analysis of six unpublished WG3 systems

In this section, we analyse six previously unpublished ESPRESSO datasets. These stars were observed in the context of the WG3, but either the data do not suffice for a robust mass measurement, or the planets were previously confirmed by teams using other facilities. Section 3.1 describes the observations, Section 3.2 the stellar parameter computation, and Section 3.3 the planet modelling.

3.1. Observations

3.1.1. ESPRESSO radial velocities

All our targets were observed with ESPRESSO in the context of the GTO WG3 transiting candidate follow-up. Table 3 lists the number of observations, time span, exposure time, and CCF mask used for the reduction for each of the targets presented in this paper. All the spectra were processed with the ESPRESSO data reduction software (DRS, Pepe et al. 2021) v.3.0.0, which computes RVs through the cross-correlation function (CCF) method (Baranne et al. 1996). The DRS also computes activity indicators: the Mount-Wilson S-index (S_{MW}, Vaughan et al. 1978) and $\log R'_{hk}$ (Noyes et al. 1984), which measure chromospheric emission in the cores of the Ca II H and K lines; the H_{α} index (Cincunegui et al. 2007; Bonfils et al. 2007), which measures it in the H_{α} line; the Na index (Díaz et al. 2007), which measures it in the Na I D1 and D2 lines; and the full width at half maximum (FWHM), bisector inverse slope (BIS, Queloz et al. 2001), and contrast of the CCF. The RVs and activity indicators were obtained from the Data & Analysis Center for Exoplanets (DACE) platform[1].

For some targets, observations were carried out both before and after ESPRESSO underwent a major intervention in June–July 2019, when the fibre link was replaced (Pepe et al. 2021). When this was the case, we split the ESPRESSO data into two sets pre- and post-upgrade, labelled ESPRESSO18 and ESPRESSO19, respectively. We treated these as independent data sets in the fitting.

3.1.2. TESS photometry

We used TESS Presearch Data Conditioning Simple Aperture Photometry (PDC-SAP) (Stumpe et al. 2012, 2014; Smith et al. 2012) photometry, which we obtained from the Mikulski Archive for Space Telescopes (MAST) archive, for TOI-266 and TOI-186. This photometry was processed by the *TESS* Science Processing Operations Center (SPOC, Jenkins et al. 2016) at NASA Ames Research Center. The resulting light curves were also searched for transit signals by SPOC (Jenkins 2002; Jenkins et al. 2010, 2020).

TOI-266 was observed in sector 3 (24 September–14 October 2018) during the TESS prime mission, and in sector 30 (23 September–20 October 2020) during the first extended mission. In both sectors it was observed in camera 1, CCD 2, in 2-minute cadence. Two potential planet candidates at ~11 d and ~20 d were identified by SPOC and designated as TESS Objects of Interest TOI-266.01 and TOI-266.02 by the TESS Science Office (Guerrero et al. 2021) on 30 November 2018.

TOI-186 was observed in sectors 1–4 (25 July–14 November 2018) during the TESS prime mission; in sectors 28–30 and 34 (31 July–20 October 2020 and 14 January–8 February 2021) during the first extended mission; and sectors 61, 64, 68, and 69 (18 January–12 February 2023, 6 April–3 May 2023, and 29 July–20 September 2023) during the second extended mission. All sectors were observed in 2-minute cadence. Sectors 1, 2, 28, 29, 69, and 69 were observed with camera 3, CCD 4; sectors 3 and 30 with camera 3, CCD 3; sector 4 with camera 4, CCD 2; sectors 34 and 61 with camera 4, CCD 3; sector 64 with camera 4,

[1] Available online at https://dace.unige.ch

Table 2. ESPRESSO WG3 planets.

Name	K (m s^{-1})	Mass ($M_\oplus$)	Radius ($R_\oplus$)	Density (g cm^{-3})	Period (d)	Eccentricity	S ($S_\oplus$)	RV jitter (m s^{-1})	Reference
GJ 9827 b	3.53 ± 0.22	$4.28^{+0.35}_{-0.33}$	$1.44^{+0.09}_{-0.07}$	7.9 ± 1.6	1.208974	0	306 ± 14	0.42	Passegger et al. (2024)
GJ 9827 c	1.06 ± 0.21	$1.86^{+0.37}_{-0.39}$	$1.13^{+0.07}_{-0.05}$	7.1 ± 2.0	3.648103	0	711.0 ± 35.4	0.42	Passegger et al. (2024)
GJ 9827 d	1.44 ± 0.27	$3.02^{+0.58}_{-0.57}$	$1.89^{+0.16}_{-0.14}$	2.46 ± 0.78	6.201812	0	665.5 ± 31.3	0.42	Passegger et al. (2024)
K2-38 b	$2.95^{+0.44}_{-0.39}$	$7.3^{+1.1}_{-1}$	1.54 ± 0.14	11.0 ± 3.4	4.01593	$0.197^{+0.067}_{-0.060}$	445.8 ± 13.9	0.96	Toledo-Padrón et al. (2020)
K2-38 c	$2.41^{+0.39}_{-0.37}$	8.3 ± 1.3	2.29 ± 0.26	3.8 ± 1.4	10.56103	$0.161^{+0.096}_{-0.078}$	122.0 ± 3.9	0.96	Toledo-Padrón et al. (2020)
K2-111 b	2.21 ± 0.32	$5.29^{+0.76}_{-0.77}$	$1.82^{+0.11}_{-0.09}$	4.8 ± 1.1	5.3518	$0.13^{+0.13}_{-0.09}$	424.7 ± 21.1	1.57	Mortier et al. (2020)
K2-111 c	$3.27^{+0.31}_{-0.32}$	†11.3 ± 1.1	–	–	15.6785	$0.07^{+0.07}_{-0.05}$	100.9 ± 4.8	1.57	Mortier et al. (2020)
K2-157 b	$1.1^{+0.39}_{-0.41}$	$1.14^{+0.41}_{-0.42}$	0.935 ± 0.09	7.7 ± 3.6	0.3652575	0	6660 ± 200	1.43	Castro-González et al. (2025)
K2-157 c	7.17 ± 0.42	†30.8 ± 1.9	–	–	25.942	<0.2	22.65 ± 0.68	1.43	Castro-González et al. (2025)
K2-157 d	$3.96^{+0.42}_{-0.41}$	†23.3 ± 2.5	–	–	66.5	<0.5	6.46 ± 0.21	1.43	Castro-González et al. (2025)
TOI-130 b	$1.93^{+0.334}_{-0.35}$	$7.8^{+1.5}_{-1.4}$	2.45 ± 0.05	2.91 ± 0.59	14.339156	$0.08^{+0.09}_{-0.05}$	132.4 ± 4.0	1.17	Sozzetti et al. (2021)
TOI-130 c	$3.17^{+0.34}_{-0.32}$	†$18.4^{+1.8}_{-1.9}$	–	–	40.87	$0.07^{+0.08}_{-0.04}$	32.8 ± 1.0	1.17	Sozzetti et al. (2021)
TOI-134 b	$3.2^{+0.29}_{-0.3}$	4.07 ± 0.45	1.63 ± 0.14	5.2 ± 1.5	1.40152604	0	167.1 ± 10.2	2.145	Hobson et al. (2024)
TOI-144 b	196.1 ± 0.7	†9.89 ± 0.25	–	–	2088.8	0	0.1427 ± 0.0045	1.2	Damasso et al. (2020)
TOI-144 c	1.5 ± 0.2	4.3 ± 0.7	2.11 ± 0.05	2.52 ± 0.45	6.267852	0	332.0 ± 10.3	1.2	Damasso et al. (2020)
TOI-174 b	$2.68^{+0.24}_{-0.25}$	$8.32^{+0.78}_{-0.79}$	$2^{+0.11}_{-0.10}$	5.7 ± 1.1	17.667087	$0.072^{+0.039}_{-0.040}$	17.60 ± 0.65	0.617	Barros et al. (2022)
TOI-174 c	0.92 ± 0.23	$3.41^{+0.88}_{-0.81}$	$1.87^{+0.12}_{-0.11}$	2.87 ± 0.92	29.79749	$0.063^{+0.054}_{-0.043}$	8.77 ± 0.31	0.617	Barros et al. (2022)
TOI-174 d	0.29 ± 0.11	$0.55^{+0.21}_{-0.20}$	$0.75^{+0.067}_{-0.057}$	7.2 ± 3.3	3.97664	$0.07^{+0.050}_{-0.047}$	128.6 ± 4.7	0.617	Barros et al. (2022)
TOI-174 e	$0.3^{+0.12}_{-0.11}$	$0.72^{+0.28}_{-0.27}$	$0.818^{+0.080}_{-0.065}$	7.2 ± 3.5	7.90754	$0.07^{+0.052}_{-0.047}$	51.4 ± 1.8	0.617	Barros et al. (2022)
TOI-174 f	0.29 ± 0.11	$0.77^{+0.44}_{-0.40}$	$1.137^{+0.084}_{-0.077}$	2.9 ± 1.8	12.1621839	$0.07^{+0.048}_{-0.051}$	28.9 ± 1.1	0.617	Barros et al. (2022)
TOI-175 b	$0.46^{+0.20}_{-0.17}$	$0.4^{+0.16}_{-0.15}$	$0.85^{+0.061}_{-0.047}$	3.6 ± 1.6	2.2531136	$0.103^{+0.117}_{-0.045}$	23.6 ± 1.9	0.895	Demangeon et al. (2021)
TOI-175 c	$2.19^{+0.17}_{-0.20}$	$2.22^{+0.26}_{-0.25}$	$1.385^{+0.095}_{-0.075}$	4.6 ± 1.1	3.6906777	$0.103^{+0.045}_{-0.058}$	12.3 ± 1.0	0.895	Demangeon et al. (2021)
TOI-175 d	$1.5^{+0.22}_{-0.19}$	1.94 ± 0.28	$1.521^{+0.119}_{-0.098}$	3.03 ± 0.83	7.4507245	$0.074^{+0.057}_{-0.046}$	4.79 ± 0.39	0.895	Demangeon et al. (2021)
TOI-175 e	$2.01^{+0.16}_{-0.20}$	†$3.06^{+0.33}_{-0.37}$	–	–	12.796	$0.128^{+0.108}_{-0.076}$	2.21 ± 0.37	0.895	Demangeon et al. (2021)
TOI-178 b	$1.05^{+0.25}_{-0.30}$	$0.96^{+0.70}_{-0.65}$	$1.2^{+0.041}_{-0.037}$	3.1 ± 2.3	1.9145601	0	194.2 ± 12.3	0.51	Leleu et al. (2021)
TOI-178 c	$2.77^{+0.22}_{-0.33}$	$4.64^{+0.52}_{-0.53}$	$1.754^{+0.032}_{-0.040}$	4.72 ± 0.63	3.238486	$0.00032^{+0.00065}_{-0.00020}$	826.9 ± 51.9	0.51	Leleu et al. (2021)
TOI-178 d	$1.34^{+0.31}_{-0.39}$	$5.2^{+0.39}_{-0.43}$	$2.695^{+0.041}_{-0.046}$	1.46 ± 0.14	6.557569	0.0068 ± 0.0016	608.4 ± 38.9	0.51	Leleu et al. (2021)
TOI-178 e	$1.62^{+0.41}_{-0.34}$	3.48 ± 0.29	$2.301^{+0.038}_{-0.039}$	1.57 ± 0.15	9.96318	$0.00038^{+0.00067}_{-0.00025}$	510.9 ± 32.9	0.51	Leleu et al. (2021)
TOI-178 f	$2.76^{+0.46}_{-0.42}$	$5.63^{+0.45}_{-0.41}$	$2.417^{+0.041}_{-0.048}$	2.19 ± 0.22	15.23335	$0.00045^{+0.00070}_{-0.00026}$	382.8 ± 24.1	0.51	Leleu et al. (2021)
TOI-178 g	$1.3^{+0.38}_{-0.59}$	$4.4^{+0.39}_{-0.37}$	$2.939^{+0.057}_{-0.055}$	0.95 ± 0.10	20.71663	$0.00043^{+0.00065}_{-0.00028}$	315.7 ± 20.3	0.51	Leleu et al. (2021)
TOI-198 b	$1.673^{+0.207}_{-0.240}$	$3.17^{+0.64}_{-0.65}$	1.36 ± 0.13	6.9 ± 2.4	10.215213	0	7.2 ± 2.4	0.005	Zapatero Osorio et al. (2026)
TOI-214 b	$0.49^{+0.17}_{-0.16}$	$1.35^{+0.46}_{-0.46}$; < 2.73	0.996 ± 0.050	7.5 ± 2.8; <15.2	9.695931	$0.035^{+0.027}_{0.018}$	71.2 ± 2.4	1.53	Benatti et al., in prep
TOI-214 c	2.3 ± 0.17	$7.88^{+0.61}_{-0.66}$	1.941 ± 0.074	5.92 ± 0.84	18.5537114	$0.095^{+0.035}_{-0.023}$	30.1 ± 1.0	1.53	Benatti et al., in prep
TOI-238 b	2.36 ± 0.32	3.4 ± 0.46	1.402 ± 0.086	6.8 ± 1.6	1.2730991	<0.18	766.4 ± 40.6	1.99	Suárez Mascareño et al. (2024)
TOI-238 c	2.46 ± 0.41	6.7 ± 1.1	2.18 ± 0.18	3.6 ± 1.1	8.465651	<0.36	64.6 ± 10.0	1.99	Suárez Mascareño et al. (2024)
TOI-244 b	1.55 ± 0.16	2.68 ± 0.3	1.52 ± 0.12	4.2 ± 1.1	7.397225	0	7.29 ± 0.37	0.19	Castro-González et al. (2023)
TOI-260 b	$1.57^{+0.59}_{-0.57}$	4.23 ± 1.6	1.71 ± 0.08	4.7 ± 1.9	13.475853	0	9.82 ± 0.39	1.51	Hobson et al. (2024)
TOI-262 b	$2.01^{+0.20}_{-0.21}$	6.59 ± 0.81	2.47 ± 0.13	2.40 ± 0.48	11.145334	0	56^{+8}_{-7}	0.008	Zapatero Osorio et al., in prep
TOI-270 b	1.27 ± 0.21	1.58 ± 0.26	1.206 ± 0.039	4.95 ± 0.95	3.3601538	0.034 ± 0.025	18.99 ± 0.46	0.68	Van Eylen et al. (2021)
TOI-270 c	4.16 ± 0.24	6.15 ± 0.37	2.355 ± 0.064	2.59 ± 0.26	5.6605731	0.027 ± 0.021	9.47 ± 0.23	0.68	Van Eylen et al. (2021)
TOI-270 d	2.56 ± 0.23	4.78 ± 0.43	2.133 ± 0.058	2.71 ± 0.33	11.379573	0.032 ± 0.023	3.734 ± 0.091	0.68	Van Eylen et al. (2021)
TOI-283 b	$1.86^{+0.58}_{-0.56}$	6.54 ± 2.04	2.34 ± 0.09	2.80 ± 0.93	17.61745	0	30.4 ± 2.5	5.11	Murgas et al. (2025)
TOI-286 b	1.98 ± 0.33	4.53 ± 0.78	1.42 ± 0.1	8.7 ± 2.4	4.5117244	0	152.5 ± 6.8	1.56	Hobson et al. (2024)
TOI-286 c	$0.79^{+0.64}_{-0.47}$	3.72 ± 2.22	1.88 ± 0.12	3.1 ± 1.9	39.361826	0	8.50 ± 0.38	1.56	Hobson et al. (2024)
TOI-455 b	2.15 ± 0.19	2.32 ± 0.25	1.43 ± 0.09	4.36 ± 0.95	5.358764	0	7.8 ± 2.9	0.88	Lavie et al. (2023)
TOI-455 c	1.11 ± 0.2	1 ± 0.19	$1.6^{+0.67}_{-0.34}$	1.3 ± 1.7	3.123898	0	15.6 ± 5.5	0.88	Lavie et al. (2023)
TOI-455 d	$1.53^{+0.40}_{-0.41}$	†$2.72^{+0.75}_{-0.75}$	–	–	24.3	0	0.98 ± 0.44	0.88	Lavie et al. (2023)
TOI-469 b	2.8 ± 0.2	9.6 ± 0.8	$3.48^{+0.07}_{-0.08}$	1.25 ± 0.14	13.63083	0	60.7 ± 2.2	0.7	Damasso et al. (2023)
TOI-469 c	2.1 ± 0.1	4.5 ± 0.3	$1.58^{+0.10}_{-0.11}$	6.3 ± 1.4	3.53796	0	365.6 ± 13.8	0.7	Damasso et al. (2023)
TOI-469 d	1.9 ± 0.1	5.1 ± 0.4	1.37 ± 0.11	10.9 ± 2.8	6.42975	0	165.0 ± 6.1	0.7	Damasso et al. (2023)
TOI-512 b	1.54 ± 0.21	$3.57^{+0.53}_{-0.55}$	1.54 ± 0.1	5.4 ± 1.3	7.18886	$0.02^{+0.06}_{-0.03}$	127 ± 9	0.79	Rodrigues et al. (2025)
TOI-713 b	$1.062^{+0.186}_{-0.179}$	$1.754^{+0.321}_{-0.326}$	$1.169^{+0.097}_{-0.099}$	6.0 ± 1.9	1.87152392922476	0	202 ± 33	0.47	Barros et al., in prep
TOI-713 c	$1.548^{+0.513}_{-0.548}$	$6.521^{+2.191}_{-2.522}$	$2.06^{+0.170}_{-0.176}$	4.1 ± 1.9	35.9994728661654	$0.26^{+0.16}_{-0.17}$	3.84 ± 0.84	0.47	Barros et al., in prep
TOI-2322 b	$0.84^{+0.97}_{-0.56}$	$2.31^{+2.67}_{-1.54}$	$0.994^{+0.057}_{-0.059}$	12.9 ± 8.9	11.30717	0	22.04 ± 5.34	4.07	Hobson et al. (2025)
TOI-2322 c	$5.37^{+1.29}_{-1.6}$	$18.1^{+4.34}_{-5.36}$	$1.874^{+0.066}_{-0.057}$	15.1 ± 4.8	20.225528	0	10.15 ± 2.5	4.07	Hobson et al. (2025)
BD+20594 b	$1.08^{+0.46}_{-0.44}$	5.2 ± 2.2; <12.0	2.23 ± 0.20	2.6 ± 1.3; <5.9	41.68547	0	23.9 ± 0.5	2.1	This work
K2-62 b	$1.77^{+0.69}_{-0.61}$	4.0 ± 1.6; <8.6	1.77 ± 0.20	4.0 ± 2.1; <8.7	6.67188	0	51.4 ± 0.9	1.805	This work
K2-62 c	$2.19^{+0.89}_{-0.92}$	6.6 ± 2.8; <14.7	2.17 ± 0.16	3.6 ± 1.7; <8.1	16.19752	0	15.8 ± 0.3	1.805	This work
K2-105 b	$1.7^{+1.2}_{-1.0}$	5.0 ± 3.5; <15.5	3.145 ± 0.073	0.88 ± 0.62; <2.74	8.2669720877	0	98.5 ± 1.9	4.595	This work
K2-105 c	$4.36^{+0.99}_{-1.04}$	†11.1 ± 2.7	–	–	5.0217295799	0	191.6 ± 3.7	4.595	This work
K2-184 b	$4.4^{+1.5}_{-1.6}$	10.9 ± 4.7; <29.8	1.216 ± 0.062	33 ± 15; <76	16.977959	$0.574^{+0.083}_{-0.090}$	33.9 ± 2.6	2.47	This work
TOI-186 b	$6.24^{+0.30}_{-0.31}$	25.94 ± 1.3	2.809 ± 0.062	6.42 ± 0.52	35.613442	0.122 ± 0.022	6.0 ± 0.1	2.43	This work
TOI-186 c	$0.57^{+0.32}_{-0.39}$	1.43 ± 0.80; <3.83	0.98 ± 0.04	8.4 ± 4.8; 22 < .4	7.789787	$0.25^{+0.20}_{-0.13}$	46.5 ± 2.6	2.43	This work
TOI-266 b	2.42 ± 0.30	7.39 ± 0.92	2.57 ± 0.12	2.39 ± 0.45	10.751014	0	101.6 ± 1.2	1.42	This work
TOI-266 c	$2.41^{+0.33}_{-0.32}$	9.0 ± 1.2	2.48 ± 0.14	3.25 ± 0.71	19.60550	0	45.6 ± 0.5	1.42	This work

Notes. Top: planets confirmed and characterised by the ESPRESSO WG3 sub-programme, listed alphabetically. For non-transiting planets, we provide the minimum mass m sin i, indicated by a prepended †. Bottom: planets for which we present either upper mass limits or parameter updates in this work. For those where we were not able to reach a 3σ measurement of the semi-amplitude, we give both the best-fit mass and density and the 3σ upper mass and density limits.

Table 3. ESPRESSO observations summary for the systems presented in this work.

Target	Observations	Time span	Exp. time (s)	CCF mask	Median RV error (m/s)
K2-184	46	6 Feb. 2019–27 Dec. 2020	600–900	K2	0.85
K2-105	40	14 Nov. 2018–27. Dec. 2020	900–1500	G9	1.11
TOI-266	26	13 Sep. 2021–19 Dec. 2022	900–1200	G8	0.51
K2-62	24	3 May 2019–14 Aug. 2021	1200–1800	K2	1.13
BD+20594	15	30 Oct. 2018–15 Sep. 2019	900	G9	1.09
TOI-186	10	30 Nov. 2019–9 Aug. 2021	900	K2	0.14

CCD 4. Two potential planet candidates at ~8 d and ~36 d were identified by SPOC and designated by the TESS Science Office as TOI-186.01 on 4 December 2018 and TOI-186.02 on 9 July 2020, respectively.

3.1.3. K2 photometry

We used K2 photometry for K2-105, K2-184, K2-62, and BD+20594. While all these targets were also observed with TESS, the photometric precision is insufficient to clearly detect the transits, so we do not include the TESS photometry in the analysis. Both K2-105 and K2-184 were observed in campaign 5, from 27 April to 10 July 2015, and in campaign 18, from 13 May to 2 July 2018. K2-62 was observed in campaign 3, from 15 November 2014 to 23 January 2015. BD+20594 was observed in campaign 5, from 8 February to 20 April 2015. For K2-62 and BD+20594, only 30-minute cadence data is available. For K2-105 and K2-184, 1-minute cadence data is available only for campaign 18; for consistency, we use the 30-minute cadence photometry for both campaigns.

3.2. Stellar parameters

The stellar parameters for all our targets are listed in Table 4. We also list in Table A.1 atmospheric stellar parameters for WG3 targets which were observed less than ten times, and which we do not analyse further due to the small number of RVs.

We obtained the stellar coordinates, proper motions, and parallaxes from *Gaia* Data Release 3 (Gaia Collaboration 2016, 2022). We used the co-added ESPRESSO spectra to compute the atmospheric parameters via spectral synthesis using the STEPARSYN code[2] (Tabernero et al. 2022). This code computes the effective temperature $T_{\rm eff}$, metallicity [Fe/H], surface gravity $\log g$, and a broadening parameter $v_{\rm broad}$ which includes both the macroturbulence ζ and the projected rotational velocity $v \sin i$. We use the $T_{\rm eff}$ to estimate spectral types from the tables of Pecaut & Mamajek (2013). Since the error bars reported by STEPARSYN represent only the internal errors, for the $T_{\rm eff}$ we add in quadrature the 2% error floor found by Tayar et al. (2022).

As an independent comparison and validation, we also obtained the atmospheric parameters via the measurement of the equivalent width of specific spectral lines, employing either (for FGK stars) the combined ARES+MOOG approach of Sousa (2014), or (for M dwarfs) the `ODUSSEAS` tool (Antoniadis-Karnavas et al. 2020). These provide $T_{\rm eff}$, [Fe/H], and $\log g$. We obtain generally compatible parameters with those computed using STEPARSYN. Regarding $T_{\rm eff}$, all values are compatible at the 1σ level save for K2-155, which lies at the edge of the range of validity for `ODUSSEAS`. Regarding [Fe/H], all values are compatible at 2σ save, again, K2-155, and TOI-1203, which is the most metal-poor FGK star in the sample. Regarding $\log g$, half the stars are compatible at the 2σ level. We also note that while the systematic errors for [Fe/H] and $\log g$ are less well studied, a conservative estimate is at the 0.1 dex level (Tabernero et al. 2022). If we add this in quadrature to the STEPARSYN errors, most [Fe/H] and $\log g$ values become compatible at the 1σ level. We adopt the STEPARSYN values for all our targets to maintain a uniform methodology across all spectral types.

To compute the masses, radii, bolometric luminosities, and stellar ages, we used the approach described in Brahm et al. (2019). Briefly, the broadband photometric measurements from *Gaia* (Gaia Collaboration 2016) and 2MASS (Skrutskie et al. 2006) are converted via the *Gaia* DR3 (Gaia Collaboration 2022) parallaxes to absolute magnitudes and subsequently compared to the `PARSEC` stellar evolutionary models (Bressan et al. 2012). We add the error floors of Tayar et al. (2022) – 5% in mass, 4% in radius, and 20% in age – in quadrature to the internal model errors.

Finally, we report the median and standard deviation of the $\log R'_{\rm hk}$ activity indicator computed from the ESPRESSO spectra. We use this to estimate the stellar rotation period $P_{\rm rot}$, following the $\log R'_{\rm hk}$–$P_{\rm rot}$ relation of Suárez Mascareño et al. (2015).

3.3. Data analysis

For each of our targets, we fit the RV and photometric data simultaneously with `juliet`[3] (Espinoza et al. 2019). This software enables the joint fitting of RVs through the `radvel` package (Fulton et al. 2018) and photometry through the `batman` package (Kreidberg 2015), incorporating Gaussian processes (GPs) via the `celerite` (Foreman-Mackey et al. 2017) and `george` (Ambikasaran et al. 2015) packages. The parameter space is explored via importance nested sampling, using the `dynesty` package (Speagle 2020).

For one-planet systems, we test circular models (henceforward 1*c*) and models with free eccentricity (henceforward 1*e*). For two-planet systems, we test circular models for the inner and outer planet individually (henceforth, in and out, respectively), and circular and free-eccentricity models for both planets together (henceforth, 2*c* and 2*e*, respectively). We also test the same models with the addition of GP detrending on the RVs (henceforward *model_gp*). To select the number of signals to fit, we generally consider only the transiting planet candidates, as there are no clear signals in the RV periodograms suggesting the presence of further planets. The exception is K2-105, with a strong signal in the RV periodogram at ~5 d that does not correspond to the transiting candidate at ~8 d.

[2] https://github.com/hmtabernero/SteParSyn/

[3] Available at https://github.com/nespinoza/juliet

Table 4. Stellar parameters of the targets under analysis.

Parameter	K2-184	K2-105	TOI-266	K2-62	BD+20594	TOI-186	Reference
Names	BD+14 1931	K2-105	BD-19 302	K2-62	BD+20 594	HD 21749	Simbad
	TIC 21244210	TIC 6892385	TIC 164767175	TIC 434094657	TIC 26123781	TIC 279741379	TESS
	–	TOI-5164	TOI-266	–	–	TOI-186	TESS
	K2-184	K2-105	–	K2-62	K2-56	–	K2
	651522834880015872	651907079835937280	5140454049422547200	2612830229101544704	58200934326315136	4673947174316727040	*Gaia* DR3
RA . . . . . (J2000)	$08^h36^m33^s.6296967664$	$08^h21^m40^s.8642457671$	$01^h44^m50^s.3157306405$	$22^h17^m27^s.4023572863$	$03^h34^m36^s.2293244264$	$03^h26^m59^s.2226450279$	*Gaia* DR3
DEC . . . . (J2000)	$+14°27'42''.967623427$	$+13°29'51''.119454268$	$-18°24'03''.266681201$	$-12°11'15''.010119450$	$+20°35'57''.269730747$	$-63°29'56''.762921534$	*Gaia* DR3
pm^{RA} (mas yr^{-1})	89.722	6.963	140.976	75.462	36.440	355.195	*Gaia* DR3
pm^{DEC} (mas yr^{-1})	–12.271	–4.878	–87.185	5.831	–51.358	–247.388	*Gaia* DR3
π . . . . (mas)	13.2175	5.0222	9.8339	8.8865	5.6384	61.2271	*Gaia* DR3
T . . . . (mag)	9.6071	11.2089	9.45661	11.3633	10.4021	6.9934	TESS
B . . . . (mag)	11.23†	12.68†	10.84†	13.51*	11.77†	9.302‡	Various^a
V . . . . (mag)	10.34†	11.75†	10.03†	12.40*	10.85†	8.143‡	Various
J . . . . (mag)	8.920	10.541	8.847	10.374	9.770	6.081	2-MASS
H . . . . (mag)	8.513	10.173	8.542	9.811	9.432	5.52	2-MASS
K . . . . (mag)	8.380	10.091	8.449	9.688	9.368	5.375	2-MASS
T_{eff} . . . . (K)	5214 ± 105	5400 ± 109	5613 ± 113	4662 ± 94	5748 ± 116	4675 ± 95	This work
Fe/H . . . . . . (dex)	−0.2 ± 0.02	0.16 ± 0.02	−0.15 ± 0.01	−0.21 ± 0.01	−0.24 ± 0.02	0.04 ± 0.02	This work
$\log g$ . . . . . . (dex)	4.6 ± 0.02	4.49 ± 0.03	4.38 ± 0.02	4.69 ± 0.02	4.32 ± 0.03	4.5 ± 0.04	This work
$V_{broad}{}^b$. (km s^{-1})	1.17 ± 0.03	1.5 ± 0.03	1.39 ± 0.01	1.13 ± 0.05	1.45 ± 0.01	1.23 ± 0.04	This work
$R_\star$ . . . . ($R_\odot$)	0.760 ± 0.031	0.887 ± 0.036	0.958 ± 0.039	0.666 ± 0.027	1.088 ± 0.045	0.709 ± 0.029	This work
$M_\star$ . . . . ($M_\odot$)	0.759 ± 0.039	0.925 ± 0.047	0.838 ± 0.042	0.667 ± 0.034	0.847 ± 0.042	0.726 ± 0.037	This work
$L_{bol,\star}$ . . . . . . ($L_\odot$)	$0.3857^{+0.0038}_{-0.0031}$	$0.5991^{+0.0109}_{-0.0088}$	$0.8203^{+0.0090}_{-0.0073}$	$0.1889^{+0.0033}_{-0.0032}$	1.183 ± 0.027	$0.2151^{+0.0033}_{-0.0032}$	This work
Age . . . . . . (Gyr)	$10.7^{+2.6}_{-2.6}$	5.1 ± 1.4	12.6 ± 2.6	$12.1^{+2.6}_{-2.9}$	13.2 ± 2.6	$10.1^{+2.6}_{-2.3}$	This work
$\log R'_{hk}$	−5.117 ± 0.339	−5.038 ± 0.035	−5.024 ± 0.122	−4.983 ± 0.046	−5.682 ± 0.18	−4.921 ± 0.028	This work
P_{rot} . . . . (d)	40.0 ± 26.0	34.0 ± 5.0	33.0 ± 9.0	31.0 ± 5.0	114.0 ± 42.0	28.0 ± 4.0	This work
Spectral type . . .	K1V	G9V	G6V	K4V	G2V	K4V	PM13

Notes. ^{a} B and V magnitude sources: †: the Tycho-2 Catalogue (Høg et al. 2000), ⋆: The Fourth US Naval Observatory CCD Astrograph Catalog (UCAC4, Zacharias et al. 2013), ‡: Koen et al. (2010). ^{b} Broadening parameter including both the macroturbulence ζ and the projected rotational velocity v sin i, as described in Tabernero et al. (2022). Other references: Simbad: Simbad astronomical database (Wenger et al. 2000); *TESS*: *TESS* Input Catalog (Stassun 2019); 2MASS: Two-micron All Sky Survey (Skrutskie et al. 2006); *Gaia* DR3: *Gaia* Data Release 3 (Gaia Collaboration 2016, 2022); PM13: using the tables of Pecaut & Mamajek (2013). The mass, radius, and T_{eff} have systematic errors added in quadrature; the error bars on [Fe/H] and $\log g$ represent only the internal errors, as the systematic errors are less well studied (see Section 3.2).

The following input parameters are required in `juliet` for joint RV and transit fits, for each planet i: period, P_i; time of transit, $t_{0,i}$; planet-to-star radius ratio, p_i; impact parameter, b_i; RV semi-amplitude, K_i; and either eccentricity, e_i, and angle of periastron, ω_i, or a derived parametrisation, such as $\sqrt{e_i}\sin\omega_i$, $\sqrt{e_i}\cos\omega_i$. We adopted the latter parametrisation, as recommended by Eastman et al. (2013). We took priors for P_i, $t_{0,i}$, p_i, and b_i from previous confirmation papers, validation papers, or Exofop, respectively. For K_i, we took a broad uniform prior of $\mathcal{U}(0, 10)\,\mathrm{ms}^{-1}$, and for $\sqrt{e_i}\sin\omega_i$, $\sqrt{e_i}\cos\omega_i$, we took broad uniform priors of $\mathcal{U}(-1, 1)$.

The following instrumental parameters are also required: for each RV instrument, the systemic radial velocity, $\mu_{\mathrm{instrument}}$, and the jitter, $\sigma_{\mathrm{w,instrument}}$; for each photometric instrument, the dilution factor, $m_{\mathrm{dilution,instrument}}$; the flux offset, $m_{\mathrm{flux,instrument}}$; the jitter, $\sigma_{\mathrm{w,instrument}}$; and the limb-darkening parameters, $q_{1,\mathrm{instrument}}$ and $q_{2,\mathrm{instrument}}$, for the quadratic law parametrisation of Kipping (2013). For $\mu_{\mathrm{instrument}}$, we took a uniform prior of $\mathcal{U}(\mathrm{RV_{min}}, \mathrm{RV_{max}})$. We fixed $m_{\mathrm{dilution,instrument}}$ to 1 as the TESS and K2 light curves are dilution corrected. For the remaining instrumental parameters, we took broad priors.

In all fits, we applied GP detrending to the photometry, for which we employed the (approximate) Matern 3/2 kernel (Foreman-Mackey et al. 2017), as implemented in `celerite`. We used a two-step process on the photometry itself, where we first masked the transits and fit GPs to the out-of-transit data only on a sector-by-sector basis, with broad log-uniform priors of $\mathcal{J}(1\times10^{-6}, 1\times10^{6})$ for $\sigma_{\mathrm{GP,sector}}$ and $\mathcal{J}(0.001, 1\times10^{3})$ for $\rho_{\mathrm{GP,sector}}$. We then used the resulting parameters as normal priors for the photometry GPs in the joint full fits. This two-step process improves the exploration of the parameter space and allows for faster convergence, as described in Patel & Espinoza (2022).

In the models that include GP detrending for the RVs, we used the quasi-periodic kernel (called exp-sine-squared kernel in `juliet`) of Haywood et al. (2014). To constrain the priors, we first fit a GP to the FWHM values, with broad log-uniform or Jeffreys priors of $\mathcal{J}(0.001, 1000)$ for $\sigma_{\mathrm{GP,FWHM}}$, $\mathcal{J}(1\times10^{-6}, 0.1)$ for $\alpha_{\mathrm{GP,FWHM}}$, and $\mathcal{J}(1\times10^{-6}, 10)$ for $\Gamma_{\mathrm{GP,FWHM}}$; along with a normal prior of $\mathcal{N}(P_{rot}, \sigma_{Prot})$ for the rotation period GP hyperparameter $P_{\mathrm{rot,GP,FWHM}}$, taking the value and error of the stellar rotation period derived in Sect 3.2 as the mean and standard deviation, respectively. We then used the resulting parameters as normal (or, in cases where a pure normal led to sampling values below zero and thus caused the fit to fail, truncated positive normal) priors for the RV GP in the joint full fits. We also applied a scaling factor to the $\sigma_{\mathrm{GP,FWHM}}$ posterior, computed as the ratio of the standard deviation of the two time series, $\sigma_{\mathrm{RV}}/\sigma_{\mathrm{FWHM}}$.

The ESPRESSO RVs were obtained from DACE, as described in Section 3.1.1. Other RVs for previously confirmed planets were taken from the respective confirmation papers. The TESS PDCSAP light curves were downloaded using the built-in `juliet` TESS MAST archive query function. The K2 light curves were downloaded using the `Lightkurve` package[4] (Lightkurve Collaboration 2018; Astropy Collaboration 2022; Ginsburg et al. 2019). We also used the built-in `Lightkurve` utilities to remove long-term trends and correct for the spacecraft motion in the K2 light curves.

[4] https://lightkurve.github.io/lightkurve/index.html

3.3.1. K2-184

This system has a single transiting planet, which was validated in Mayo et al. (2018) and Livingston et al. (2018). The K2 transits show significant TTVs, as reported by Castro-González et al. (2022). However, we see no significant signals in the RVs that could help constrain the body causing the TTVs, so we do not analyse them further. We note that Castro-González et al. (2022) were unable to derive a TTV period due to an insufficient coverage, with only linear trends being found in the two K2 campaigns, which were observed three years apart. The RV data, meanwhile, span a little under two years, though the majority of it (38 of the 46 data points) was obtained in the first four months.

We tested the $1c$, $1e$, $1c\_gp$, and $1e\_gp$ models on the ESPRESSO RVs and K2 photometry. Both with and without GP detrending, the eccentric model is significantly favoured over the circular model, with $\Delta \log Z_{1e-1c} \approx 2-3$. Likewise, the GP detrending is significantly favoured, with $\Delta \log Z_{1c\_gp-1c} \approx 8$, $\Delta \log Z_{1e\_gp-1e} \approx 7$. We thus adopt the $1e\_gp$ model as our final model, and report the priors and posteriors in Table B.1. The RVs and phase-folded light curves are shown in Figs. B.7 and B.1, respectively. K2-184 b has a $16.977959^{+0.000089}_{-0.000090}\,d$ period, $1.216 \pm 0.062\,R_\oplus$ radius, and $0.574^{+0.083}_{-0.090}$ eccentricity. We caution that this high-eccentricity fit may be driven by a residual RV signal from the body causing the TTVs, although no significant signals emerge in the residual RV periodogram. Regarding the planet's mass, we find a best-fit value of $10.9 \pm 4.7\,M_\oplus$. However, we only reach a ~2.7σ precision on the semi-amplitude, so we also provide an upper mass limit of $M_b < 29.8\,M_\oplus$.

3.3.2. K2-105

This system has a single transiting planet, validated in Narita et al. (2017). There is no signal in the RVs at the ~$8\,d$ period of this planet, but there is a strong signal at ~$5\,d$. We therefore considered this as a potential two-planet system, and tested the *in*, *out*, $2c$, and $2e$ models on the ESPRESSO RVs and K2 photometry, and with the addition of the Subaru HDS RVs from Narita et al. (2017). To constrain the priors of the potential inner planet, we ran a circular fit with `juliet` on the RVs alone, and allowed its impact parameter to go above 1 in the full fits to reflect the fact it does not appear to transit, with no signal at ~$5\,d$ in the K2 photometry BLS. Given the already complex nature of the system, we decided not to include GP detrending.

The $2c$ model is favoured in both cases, with $\Delta \log Z_{2c-in} \approx 372$, $\Delta \log Z_{2c-out} \approx 6$, and $\Delta \log Z_{2c-2e} \approx 26$ for the ESPRESSO+K2 dataset, and $\Delta \log Z_{2c-in} \approx 370$, $\Delta \log Z_{2c-out} \approx 3$, and $\Delta \log Z_{2c-2e} \approx 20$ for the full dataset. We therefore adopt the $2c$ model from the joint dataset as our final model, and report the priors and posteriors in Table B.2. The RVs and phase-folded photometry are shown in Figs. B.8 and B.3, respectively. The newly discovered inner planet K2-105 c does not transit, with the best-fit transit model being compatible with a flat line. It has a $5.02173^{+0.00042}_{-0.00065}$ d period, and a $11.1 \pm 2.7\,M_\oplus$ minimum mass. The previously validated outer planet K2-105 b has a $8.2669721^{+0.0000082}_{-0.0000077}$ d period, a $3.145 \pm 0.073\,R_\oplus$ radius, and a $5.0 \pm 3.5\,M_\oplus$. As we only reach a ~1.7σ precision on the semi-amplitude of this planet, we also report an upper mass limit of $M_b < 15.5\,M_\oplus$.

3.3.3. TOI-266

This system has two transiting planets that were previously confirmed in Akana Murphy et al. (2023), using 95 RVs from the Keck Observatory High Resolution Echelle Spectrometer (HIRES, Vogt et al. 1994). We first tested the *in*, *out*, $2c$, $2e$, and corresponding *_gp* models on the ESPRESSO RVs and TESS photometry. Both with and without detrending, the best model is that with two circular planets, and the addition of the GP is not favoured, with $\Delta \log Z_{2c\_gp-2c} \approx 0.8$. For the models without detrending, we have $\Delta \log Z_{2c-in} \approx 51$, $\Delta \log Z_{2c-out} \approx 70$, and $\Delta \log Z_{2c-2e} \approx 4$. We then tested the *in*, *out*, $2c$, and $2e$ models on the joint ESPRESSO and HIRES RV dataset together with the test photometry. Once again, the best model is that with two circular planets, with $\Delta \log Z_{2c-in} \approx 63$, $\Delta \log Z_{2c-out} \approx 87$, and $\Delta \log Z_{2c-2e} \approx 3$. We adopt the $2c$ model for the joint dataset as our final model, and report the priors and posteriors in Table B.3. The RVs and phase-folded light curves are shown in Figs. B.9 and B.4, respectively. TOI-266 b has a $10.751014^{+0.000053}_{-0.000058}$ d period, $2.57 \pm 0.12\,R_\oplus$ radius, and $7.39 \pm 0.92\,M_\oplus$ mass, while TOI-266 c has a 19.60550 ± 0.00018 d period, $2.48 \pm 0.14\,R_\oplus$ radius, and $9.0 \pm 1.2\,M_\oplus$ mass. Our results are comparable to those of Akana Murphy et al. (2023), with compatible RV semi-amplitude values with improved precision, and thus improved precision on the planetary masses, as shown in Table 5. Our masses are systematically smaller as a result of a lower stellar mass of $0.838 \pm 0.042\,M_\odot$, compared to $0.91 \pm 0.06\,M_\odot$ from Akana Murphy et al. (2023).

Table 5. TOI-266 semi-amplitudes and masses, from Akana Murphy et al. (2023) and this work.

Parameter	Akana Murphy et al. (2023)	This work
K_b (m s^{-1})	2.42 ± 0.53	2.42 ± 0.30
M_b ($M_\oplus$)	7.8 ± 1.8	7.39 ± 0.92
K_c (m s^{-1})	2.40 ± 0.55	$2.41^{+0.33}_{-0.32}$
M_c ($M_\oplus$)	9.40 ± 2.20	9.0 ± 1.2

3.3.4. K2-62

This system has two validated transiting planets, published in Mayo et al. (2018). We tested the *in*, *out*, $2c$, $2e$, and corresponding *_gp* models on the ESPRESSO RVs and K2 photometry. The RVs show a strong long-term trend, which we include in all models as an additional linear term given by the $rv_{intercept}$ and rv_{slope} parameters. The two-planet models are significantly favoured over both one-planet models, with $\Delta \log Z_{2c-in} \approx 167$ and $\Delta \log Z_{2c-out} \approx 404$. Without detrending, the $2e$ model is marginally but not significantly favoured ($\Delta \log Z_{2e-2c} \approx 0.4$). With GP detrending, the best model is $2c\_gp$, but it is not favoured over the no-detrending model, with $\Delta \log Z_{2c-2c\_gp} \approx 6$. We therefore adopt the $2c$ model as our final model. The priors and posteriors are given in Table B.4, and the RVs and phase-folded photometry shown in Figs. B.10 and B.5, respectively. K2-62 b has a $6.67188^{+0.00024}_{-0.00026}$ d period, a $1.77 \pm 0.20\,R_\oplus$ radius, and a $3.98 \pm 1.55\,M_\oplus$ best-fit mass, while K2-62 c has a 16.19752 ± 0.00081 d period, a $2.17 \pm 0.16\,R_\oplus$ radius, and a $6.6 \pm 2.8\,M_\oplus$ best-fit mass. Since we do not reach a 3σ measurement of the semi-amplitude for either planets, we also report upper limits for the planetary masses of $<8.6 M_\oplus$ and $<14.7\,M_\oplus$, respectively.

3.3.5. BD+20954

This system has one confirmed transiting planet (Espinoza et al. 2016, as K2-56 b), with a mass measurement using 23 HARPS

(Mayor et al. 2003) RVs. We tested 1*c* and 1*e* models for both the ESPRESSO RVs and K2 photometry alone, and including the HARPS RVs. We removed three ESPRESSO points with large error bars of $>2\,\mathrm{m\,s^{-1}}$. In both cases, the eccentric models are marginally but not significantly favoured, with $\Delta \log Z_{1e-1c} \approx 0.8$ for the fit with only ESPRESSO RVs, and $\Delta \log Z_{1e-1c} \approx 0.6$ when the HARPS RVs are included. We also tested the 1*c_gp* and 1*e_gp* models on the ESPRESSO RVs and K2 photometry, but the inclusion of the GP detrending was not favoured, with $\Delta \log Z_{1c-1c\_gp} \approx 0.4$, $\Delta \log Z_{1e-1e\_gp} \approx 1$.

We adopted as our final model the 1*c* model from the fit to the K2 photometry and joint ESPRESSO and HARPS RVs. The priors and posteriors are reported in Table B.5, and the RVs and phase-folded photometry shown in Figs. B.11 and B.2, respectively. BD+20954 b has a $41.68547^{+0.00097}_{-0.00094}$ d period and a 2.23 ± 0.20 radius. We find a notably smaller semi-amplitude than was previously reported, with $K = 1.08^{+0.46}_{-0.44}\,\mathrm{ms^{-1}}$, compared to the $3.1 \pm 1.1\,\mathrm{ms^{-1}}$ found by Espinoza et al. (2016), leading to a $5.2 \pm 2.2\,M_{\oplus}$ mass, much lower than the previous $16.3^{+6.0}_{-6.1}\,M_{\oplus}$ measurement. As we do not reach a 3σ significance on the semi-amplitude, we also give an upper mass limit of $M_b < 12.0\,M_{\oplus}$.

3.3.6. TOI-186

This system has two transiting planets, for which Dragomir et al. (2019) obtained a mass measurement for the outer planet (we stress that this is planet b, having been previously validated in Trifonov et al. 2019), and an upper mass limit for the inner (planet c, being detected later) with 55 HARPS and 225 PFS RVs (Crane et al. 2010). We first tested the *in*, *out*, 2*c*, and 2*e* on the ESPRESSO RVs and TESS photometry. Given the quantity of TESS sectors observed for this target, fitting their instrumental parameters and GPs together with the planet(s) becomes computationally unfeasible. Therefore, we adopted a variant of our two-step process, in which the values obtained for the fit to the out-of-transit data are fixed in the full fit, which is performed on the in-transit data only. The two-planet models are significantly favoured over both one-planet models, with $\Delta \log Z_{2c-in} \approx 1011$ and $\Delta \log Z_{2c-out} \approx 71$. The 2*c* model is favoured over the 2*e* model, with , with $\Delta \log Z_{2c-2e} \approx 1$. We do not apply GP detrending on the RVs in this case, as the ESPRESSO RVs are few.

We then tested the same four models on the TESS photometry and joint RV dataset including the new ESPRESSO RVs and the published HARPS and PFS RVs. We likewise do not apply GP detrending, as the joint dataset has only one common activity indicator, H_α, which shows systematic offsets and scaling differences between the three instruments. In this case, the 2*e* model was favoured, with $\Delta \log Z_{2e-2c} \approx 11$. We adopt this model as our final model; the priors and posteriors are given in Table B.6, and the RVs and phase-folded photometry shown in Figs. B.12 and B.6, respectively. TOI-186 b has a 35.613442 ± 0.000016 d period, $2.809 \pm 0.062\,R_{\oplus}$ radius, and 0.122 ± 0.022 eccentricity, while TOI-186 c has a $7.789787^{+0.000018}_{-0.000013}$ d period, $0.984 \pm 0.038\,R_{\oplus}$ radius, and $0.25^{+0.20}_{-0.13}$ eccentricity. Our mass values are in agreement with the previous results; we improve the mass error bars on the outer planet TOI-186 b slightly, going from a literature value of $M_b = 22.7^{+2.2}_{-1.9}\,M_{\oplus}$ to $M_b = 25.9 \pm 1.3\,M_{\oplus}$, but similarly to Dragomir et al. (2019) do not reach a 3σ measurement of the mass of TOI-186 c (best-fit value: $1.43 \pm 0.80\,M_{\oplus}$), and so give an upper mass limit of $M_c < 3.83\,M_{\oplus}$.

4. Population analysis

In this section, we analyse the entire population of planets discovered by the WG3 sub-programme as presented in Section 2, including both published systems, and systems with dedicated publications in preparation. We also include the six systems presented in Section 3.3. We highlight that of the 65 planets listed in Table 2, seven have only upper mass limits, and are therefore excluded from any analysis involving the planetary masses. Likewise, eight are non-transiting companions to transiting planets, and are thus excluded from any analysis involving the planetary radii. This leaves a final total of 51 transiting planets with well-determined masses and radii.

To place our systems in a global population context among other well-characterised small planets, we use the PlanetS catalogue (Otegi et al. 2020; Parc et al. 2024) to select all published planets with precisely measured masses and radii (mass measured to better than 25%, radius to better than 8%, as per the catalogue criteria), and set upper limits of $M_p \leq 40\,M_{\oplus}$ and $R_p \leq 4\,R_{\oplus}$, recovering a total of 182 planets. We then remove 23 WG3-detected planets that fall within the PlanetS criteria from the catalogue sample to avoid duplication. These planets correspond to ≈13% of the PlanetS small planet sample. We also note that 75% of the WG3 transiting planets fulfil the PlanetS catalogue criteria on mass and radius precision.

4.1. Planetary composition and insolation

Thanks to the precisely determined masses and radii derived from the ESPRESSO RVs, complementary RVs, and transit photometry, we can analyse the composition of the WG3 population. These planets span a large range of compositions, from Mercury-like through rocky to likely possessed of extended atmospheres. One of the goals of the WG3 was to examine specifically the 50–200 $S_{\oplus}$ insolation range to study the transition from rocky super-Earths to volatile-rich sub-Neptunes and search for mass thresholds at which significant evaporation of the planetary envelopes occurs. This insolation regime corresponds to that at which the radius valley was initially detected (Fulton et al. 2017); we explore the radius valley further in Section 4.2.

We plot the planets on mass-radius diagrams, together with the composition curves of Zeng et al. (2019) (for rocky planets) and Luo et al. (2024) (for volatile-rich planets), in Fig. 2 for three insolation regimes: $S_p < 50\,S_{\oplus}$, $S_p = 50 - 200\,S_{\oplus}$, and $S_p > 200\,S_{\oplus}$. We also show the planets from the PlanetS catalogue. As can be seen from the subplots in Fig. 2, while in the high-insolation and low-insolation regimes there is no clear mass threshold for the rocky to volatile-rich transition, there appears to be one at $M_p \approx 6\,M_{\oplus}$ in the medium-insolation regime, with planets below this mass generally falling on rocky composition curves, and planets above this mass being volatile-rich. We caution that this observation is based on a small number of planets; a larger sample would be needed for a more robust detection. While all our sub-samples are inherently biased, as they consist of transiting planets, the upper mass threshold for rocky planets in the medium insolation regime should be robust, as for the same radius and period (and thus same transit probability, and same insolation for the same host star) a more massive planet is easier to detect than a low-mass one.

The lack of a clear threshold mass in the low-insolation regime, where planets of both composition types can be found essentially across the entire planetary mass range, is likely due to more of these planets being hosted by low-mass stars: 51% are hosted by stars with $M_\star \leq 0.6\,M_{\odot}$, compared to 6% in the

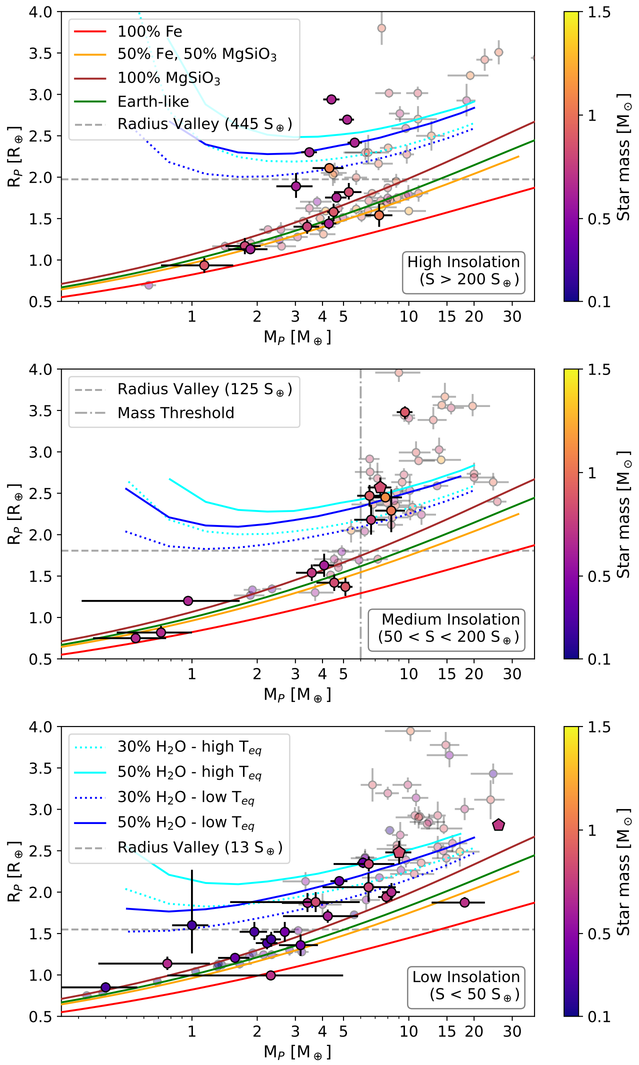

Fig. 2. Mass–radius diagrams across three insolation regimes for the WG3 planets (solid points) and small planets from the PlanetS catalogue (semi-transparent points). Planets presented in this paper are shown as pentagons. All the planets are coloured by host star mass. The coloured curves show the composition models of Zeng et al. (2019) (rocky planets) and Luo et al. (2024) (volatile-rich planets). For the latter, we show the models for the temperatures above and below the mean T_{eq} for each panel, labelled as high and low T_{eq}; these correspond to 1400 K and 1000 K for the top panel, 1000 K and 700 K for the middle panel, and 700 K and 400 K for the bottom panel. Dashed horizontal grey lines indicate the location of the radius valley at the median insolation for each population, as defined by Ho & Van Eylen (2023). The dash-dotted vertical grey line in the central plot shows a tentative threshold mass between rocky and volatile-rich planets in the medium insolation regime.

high-insolation regime and 9% in the mid-insolation regime. It has been shown (Venturini et al. 2024; Parc et al. 2024) that the radius valley (generally considered a gap between rocky super-Earths and volatile-rich sub-Neptunes) fades for M dwarfs, so this population is difficult to compare directly to that hosted by FGK stars. Alternatively, it could be related to the insolation itself; there is an emerging population of volatile-rich low-density super-Earths, that are more frequently detected in low-irradiation environments (Castro-González et al. 2023). We also note that many of the WG3 planets in this regime have comparatively large uncertainties on their masses, due to their longer orbital periods and later-type (and thus fainter) host stars.

For the high-insolation regime, there is likely a combination of host-star and irradiation effects at play. On the one hand, most of the low-mass volatile-rich planets in this regime are hosted by low-mass stars; for instance, the four WG3 planets at or above the 50% H_2O line, which are are TOI-178 d through g, orbiting a late K dwarf (Leleu et al. 2021, 2024). On the other, in this high-insolation regime we can expect both stripping of primordial atmospheres from more massive cores than in the medium-insolation case, leading to more massive planets with rocky compositions, and puffing up of volatile atmospheres, leading to larger radii for similar masses. A particularly notable feature in this regime is the massive rocky planet population, reaching to $\approx 10\,M_{\oplus}$. We do not find a similar population in the lower-insolation regimes, suggesting that rather than having a direct formation pathway, these planets are stripped cores: they accrete a significant envelope during formation, which is retained in the lower-insolation environments, but can be lost due to photo-evaporation in high-irradiation environments.

For many of the planets presented in this paper specifically, we do not achieve 3σ measurements of the semi-amplitudes. Thus, in Section 3.3 we report the standard 3σ upper mass limits. Once we take into account the radii measured from the photometry, however, we find that in the case of K2-184 b and TOI-186 c, these mass upper limits lead to unphysically dense planets with densities higher than pure iron. To obtain more physically motivated upper mass limits for these planets, we calculated the mass value of the Zeng et al. (2019) pure-iron model for the 3σ upper limit on their radii. Table 6 lists these upper mass limits, together with the initial upper mass limits derived from the `juliet` fits for comparison.

Table 6. Physically motivated upper mass limits.

Planet	Best-fit mass	3σ limit	Pure iron limit
K2-184 b	$10.87 \pm 4.68\,M_{\oplus}$	$< 29.8\,M_{\oplus}$	$<8.59\,M_{\oplus}$
TOI-186 c	$1.43 \pm 0.80\,M_{\oplus}$	$< 3.83\,M_{\oplus}$	$<3.04\,M_{\oplus}$

Another way to study the planetary compositions is through interior structure modelling. We used the ExoMDN code (Baumeister & Tosi 2023)[5] to carry out rapid uniform interior structure modelling for the full WG3 sample. ExoMDN employs mixture density networks to perform interior inference modelling, fitting a four-layer model consisting of an iron core, a silicate mantle, a water layer, and a H/He atmosphere from the planet's mass, radius, and equilibrium temperature. The outputs are mass fractions, w_{layer}, radius fractions, d_{layer}, and posterior distributions of these values, for each of the four layers. Figures C.1 and C.2 show the output mass and radius fraction posterior distribution histograms for the WG3 sample, ordered by core mass fraction and core radius fraction, respectively. We also show the results for the Earth and Neptune as comparison points. Our outputs range from dense, core-rich planets, through Earth-like compositions, intermediate cases with large water fractions, to Neptune-like gas-rich planets.

To compare the mass and radius layer fractions to the results of the same model for Earth-like and Neptune-like planets, as

[5] Available at https://github.com/philippbaumeister/ExoMDN

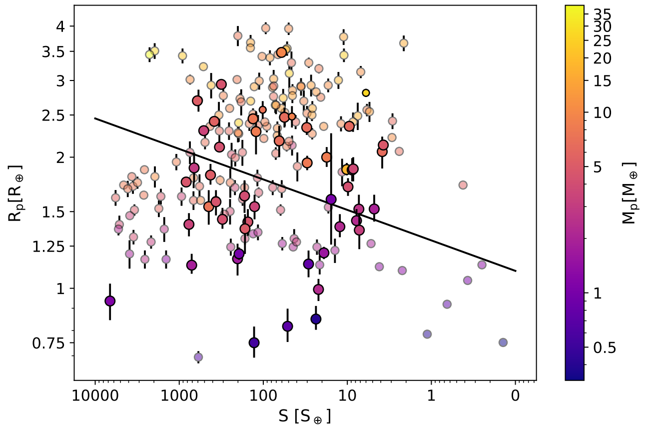

Fig. 3. Insolation-radius diagram for the WG3 planets (solid circles) and PlanetS catalogue small planets (semi-transparent circles). The planets are coloured by planet mass. The black line shows the insolation-dependent radius valley from Ho & Van Eylen (2023).

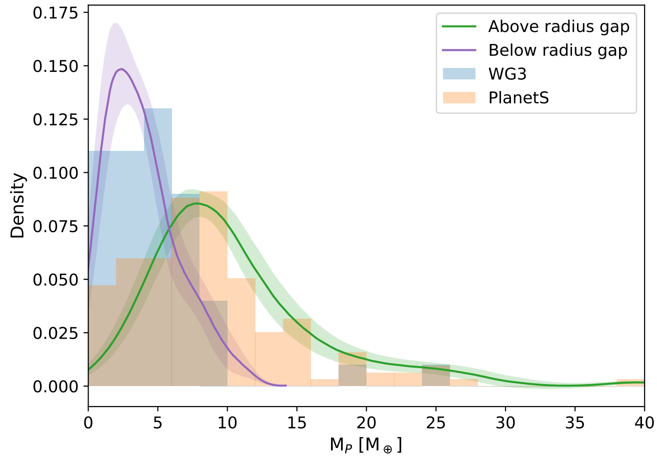

Fig. 4. Kernel density estimations of the mass distributions for the planets above (green) and below (purple) the radius gap. The shaded purple and green regions show the 1σ region. The blue and orange histograms show the mass distributions for the WG3 and PlanetS samples, respectively.

presented in Baumeister & Tosi (2023)[6], we computed the four-dimensional Euclidean distances between each planet's mass (radius) layer fractions and the mass (radius) layer fractions of Earth and Neptune, respectively. Around 56% of the sample (28 planets) are closer to Earth-like than Neptune-like values in both mass and radius, while 30% (15 planets) are closer to Neptune-like values. The remaining 14% (7 planets) are an intermediate case, closer to the Neptune model in mass fractions but to the Earth model in radius fractions. All these planets have relatively low core fractions ($w_{core} \approx 0.21$–0.40, $d_{core} \approx 0.33$–0.42), high mantle ($w_{mantle} \approx 0.31$–0.37, $d_{mantle} \approx 0.21$–0.29) and water ($w_{water} \approx 0.21$–0.40, $d_{water} \approx 0.21$–0.33) fractions, and low gas fractions ($w_{gas} \approx 0$, $d_{core} \approx 0.03$–0.14). The high water fractions suggest these planets could be water worlds. Inspecting the position of the planets in each of the three groups compared to composition tracks on the mass-radius diagram, we find that those closer to Earth-like values correspond well to rocky models, while the intermediate and Neptune-like planets fall on volatile-rich tracks.

4.2. The radius valley

One of the most remarkable features of the small planet population is the radius valley or radius gap, an underdensity of planets in the 1.5−2 $R_\oplus$ region, first identified by Fulton et al. (2017). Many mechanisms have been invoked to explain the valley, from core-powered or XUV-driven mass loss (Petigura et al. 2022; Ho & Van Eylen 2023), to in situ rocky planet versus ex situ water-rich planet formation (Venturini et al. 2020; Burn et al. 2024). The location and depth of the valley also depends on parameters such as stellar host mass (Petigura et al. 2022; Luque & Pallé 2022; Venturini et al. 2024; Parc et al. 2024) and planet insolation (Ho & Van Eylen 2023). We show the planetary radius distribution as a function of insolation for the WG3 and PlanetS planets in Fig. 3, overplotting the insolation-dependent gap derived by Ho & Van Eylen (2023). We do not attempt to re-estimate the location of the valley because our sample has non-uniformly-derived radii and insolation, and it has been shown that uniformly deriving the radii increases the depth of the valley and improves its localisation (Van Eylen et al. 2018). The separation between the two populations is clearest at mid-to-high insolations, while at low insolations several planets overlap the gap. This is also consistent with the mass-radius diagrams for different insolation regimes shown in Fig. 2, where for high and medium insolations the radius valley generally separates the rocky and volatile-rich populations, while for low insolation the separation is less clear.

The planets below the radius gap appear to be less massive and span a narrower mass range than those above the gap, a feature of this population that was previously noted in Armstrong et al. (2025). To better examine this mass bimodality, we compute the kernel density estimations (KDE) for the masses of the planets below and above the gap. Since the planet masses have associated uncertainties, to take these into account, we adopted a similar methodology to that described in Parc et al. (2024). We created 1000 samples, took a random value from a Gaussian with parameters $\mu = M_p$, $\sigma = \sigma_{M_p}$ for each planet, and recomputed the KDE for each sample. We then took the median and standard deviation of these KDEs as our final distributions and their associated errors.

Figure 4 shows these final distributions for the masses of the planets below and above the gap, together with the mass histograms for the WG3 and PlanetS samples. It can be seen that the planets below the gap span a narrow ≈0.3–10 $M_\oplus$ mass range. In agreement with Armstrong et al. (2025), we also find a sharp mass cut-off at ≈10 $M_\oplus$ for the planets below the gap; our overall distribution for these planets, however, appears more sharply peaked, and peaks at a lower value of 2.5 $M_\oplus$ compared to their broad peak at 4 $M_\oplus$. For the planets above the gap, meanwhile, we find a similar broad distribution to Armstrong et al. (2025), with a ≈1–40 $M_\oplus$ mass range, and peaking at 7 $M_\oplus$. We note that the PlanetS sample has more restrictive criteria on the errors in mass and radius than that applied by Armstrong et al. (2025), who took all planets in the Exoplanet Archive with mass and radius determinations better than 3σ; conversely, our sample extends out to planets with masses up to 40 $M_\oplus$, while they cut off at 20 $M_\oplus$. The two KDEs intersect at ≈6 $M_\oplus$, in line with our tentative rocky-volatile transition threshold presented in Section 4.1. It is also clear from Fig. 4 that ESPRESSO is a major contributor to the precise mass measurements of the

[6] Earth: $w_{core} \approx 0.74$, $w_{mantle} \approx 0.19$, $w_{water} \approx 0.06$, $w_{gas} \approx 0$; $d_{core} \approx 0.69$, $d_{mantle} \approx 0.14$, $d_{water} \approx 0.09$, $d_{gas} \approx 0.05$. Neptune: $w_{core} \approx 0.18$, $w_{mantle} \approx 0.21$, $w_{water} \approx 0.26$, $w_{gas} \approx 0.27$; $d_{core} \approx 0.22$, $d_{mantle} \approx 0.14$, $d_{water} \approx 0.16$, $d_{gas} \approx 0.46$.

below-the-gap planets, which is only to be expected as their small masses require ESPRESSO's exquisite RV precision.

4.3. Exploring the mass-metallicity correlation

The correlation between stellar metallicity and planet occurrence has been greatly explored in the literature. It is generally accepted that there is a strong giant planet occurrence–metallicity correlation (Gonzalez 1997; Santos et al. 2001; Udry & Santos 2007; Sousa et al. 2021, and references therein), and a weaker superEarth occurrence–metallicity correlation (Zhu & Dong 2021; Sousa et al. 2021, and references therein). This correlation is due to the stellar metallicity acting as a proxy for the amount of solids in the protoplanetary disk; to form large planets, more solids – and thus a higher stellar metallicity – are required (e.g. Ida & Lin 2004; Chen et al. 2025). The question then arises of whether planetary mass also correlates with metallicity, as more massive planets would require more solids available for their formation.

In Fig. 5, we show the planet mass-stellar metallicity distribution for the combined WG3 and PlanetS sample. The overall metallicity distribution is centred on solar values, with a mean of $\mu_{\rm Fe/H} = -0.05$ and a standard deviation of $\sigma_{\rm Fe/H} = 0.22$. The shape of this distribution is similar to that predicted by core-accretion models for small planets (Chen et al. 2025), providing empirical support for a core-accretion formation. We note a scarcity of planets at very low metallicities (Fe/H $\lesssim -0.5$), consistent with the observational metallicity cut-off seen both for giant planets (Mortier et al. 2012) and, more recently, in the TESS small planet sample (Boley et al. 2024). The maximum mass likewise increases with metallicity, an effect first noted by Courcol et al. (2016); ten years later, our sample remains consistent with their upper boundary. The observed small planet occurrence likewise drops off at higher metallicities; this is likely due to the higher probability of forming large planets around metal-rich stars, which inhibit the formation of small planets or dynamically eject them (Zhu & Dong 2021, and references therein).

The contour plot in Fig. 5 highlights a tendency for the more massive planets to be hosted by the more metal-rich stars. A simple linear regression with the `SciPy` package (Virtanen et al. 2020) yields a correlation with high statistical significance, with $p-value = 1.01 \times 10^{-5}$. However, both the masses and metallicities have significant error bars. We therefore use the `linmix` package (Kelly 2007)[7] to perform a linear regression taking into account the errors, using a Gaussian mixture model and MCMC sampling. The resulting median fit, which is shown in Fig. 5, is indistinguishable from that derived with `SciPy`. Taking the median and standard deviation of the MCMC samples as the values and errors of the coefficients, our fit is given by

$$\text{Mass} = (8.6 \pm 2.0) \times [\text{Fe/H}] + (8.15 \pm 0.38). \quad (1)$$

This trend is consistent with our initial hypothesis, that more massive planets would preferentially be found around more metallic stars.

Both the PlanetS catalogue metallicities, and those for the WG3 sample, are taken from the planet discovery and characterisation papers, and are thus inhomogeneous. We therefore query the SWEET-Cat catalogue of homogenous stellar parameters (Santos et al. 2013; Sousa et al. 2021) to obtain uniformly derived metallicities for our sample. Only three stars (TOI-713, TOI-214, and TOI-283) are not found in SWEET-Cat. We also verify the source of the metallicities; 70% of the WG3 sample and 63% of the PlanetS sample have metallicities homogenously derived from archival spectra, while the rest are from the literature. Repeating the linmix modelling with the SWEET-Cat metallicities, our new median fit is given by

$$\text{Mass} = (7.2 \pm 1.9) \times [\text{Fe/H}] + (7.91 \pm 0.40). \quad (2)$$

This is indistinguishable from the previous fit, showing that our population-level results are robust to inhomogeneities in the individual metallicities. Likewise, we test whether the ≈40 $M_\oplus$ planet from the PlanetS sample (TOI-849 b, Armstrong et al. 2020) is driving the trend, finding that our fits are robust to its removal.

A tentative three-dimensional correlation between mass, metallicity, and period was previously presented by Sousa et al. (2019, 2021). As our sample consists only of transiting planets, we are heavily biased towards short periods, so we do not perform an analogous three-dimensional fit. Comparing the multiplicative coefficients on the metallicity, $a \times$ [Fe/H], our value of $a = 8.6 \pm 2.0$ is lower than the $a = 13.4 \pm 0.4$ found by Sousa et al. (2021); however, the overall conclusion that masses increase with higher metallicity remains.

4.4. Comparing planet masses to typical protoplanetary disk masses

Planets form in protoplanetary disks, and so their masses (and, for multiplanetary systems, the sum of the planets' masses) cannot exceed that of the disk they formed in. This seemingly obvious statement has actually driven a large number

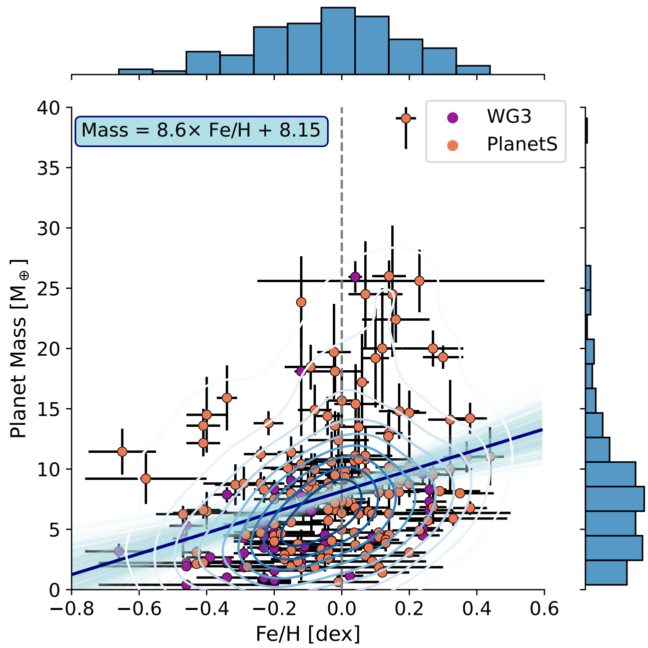

Fig. 5. Stellar metallicity versus planet mass for the WG3 planets (purple points) and small planets from the PlanetS catalogue (orange points), with contour lines in blue. Marginalised histograms of the metallicity and mass are shown on the top and right, respectively. The translucent light blue lines show random draws from the `linmix` MCMC sampling, and the solid navy line shows the median model, whose values are annotated in the blue box. The vertical dashed grey line shows the solar metallicity.

[7] Ported to Python at https://github.com/jmeyers314/linmix

of works, as comparing disk masses and planetary masses is a non-trivial endeavour: the exoplanet population is biased in complex ways and determining disk masses from continuum observations requires several assumptions on factors such as temperature, dust-to-gas-ratio, and dust optical depth (e.g. Manara et al. 2023). Recent studies suggest planets must either form early, in the more massive Class 0 and I disks (Tychoniec et al. 2020), or with formation efficiencies close to 100% if they form in Class II disks (Mulders et al. 2021).

To compare the masses of the rocky planets that constitute the combined WG3 and PlanetS sample presented in this paper to the likely mass of the disk in which they formed, we obtained a large sample of observationally determined Class II protoplanetary disk masses, together with the masses of their host stars, from Manara et al. (2023). The top panel of Fig. 6 shows the sum of planet masses for each system, and the protoplanetary disk masses, as a function of stellar masses. The middle and bottom panels show the ratio between the sum of planet masses and the median and maximum disk masses, respectively, with these computed in a 0.1 $M_\odot$ bin around the mass of the planet's host star. We included disk upper mass limits in this computation, as these correspond to disks that are not detected at mm wavelengths but whose existence is inferred from other observations such as IR excess. To exclude them would then bias our median masses towards higher masses. The summed planet masses generally represent only ~5% of the maximum disk mass for their stellar type, but they are very similar to the median disk masses overall. This suggests they must either form with a very high efficiency, form preferentially in more massive disks, or form earlier in the disk's lifetime. Likewise, the detected planets represent only a lower limit on the total planetary mass in the system; there could be additional planets on wide or misaligned orbits that are not detectable with the current data, increasing the total planet mass and further strengthening our argument.

It is also worth noting that the disks in the sample of Manara et al. (2023) come from low-mass (and consequently not particularly irradiated) star-forming regions, which are not the norm for Galactic star-formation environments (Lada & Lada 2003; Fatuzzo & Adams 2008; Winter & Haworth 2022). We generally do not know the formation environments of our present-day planet-hosting stars. If they formed in higher-mass regions, which are more densely populated and contain more OB stars, the strong UV radiation environment is expected to have caused strong, rapid photo-evaporation of the protoplanetary disks (Störzer & Hollenbach 1999; Scally & Clarke 2001; Haworth et al. 2018, 2023), with the effect being particularly pronounced for low-mass disks (Qiao et al. 2026). This further supports early planet formation and/or preferential formation in more massive disks.

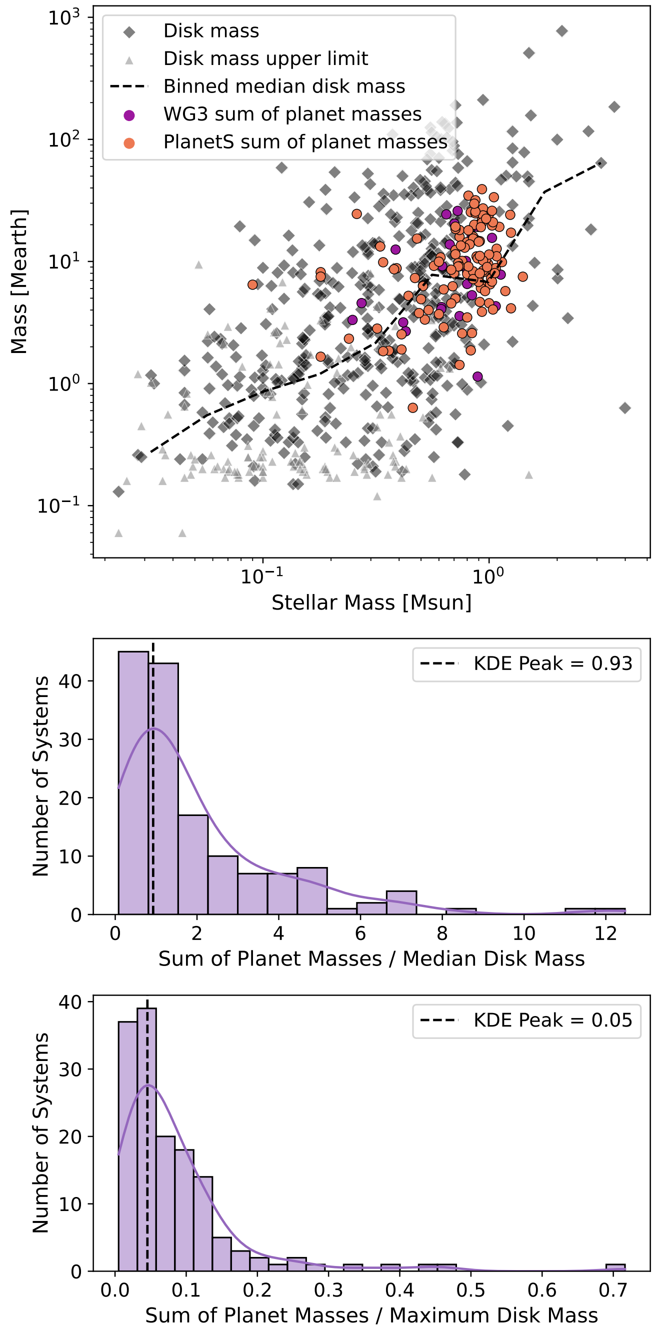

Fig. 6. Planet and protoplanetary disk mass comparison. Top: stellar mass versus sum of planet masses for the WG3 sample (purple points) and small planets from the PlanetS catalogue (orange points), and versus protoplanetary disk masses (grey squares) and disk mass upper limits (light grey triangles). The black dashed line shows the median disk mass over ten stellar mass bins. Middle: sum of planet masses to median disk mass ratio histogram and KDE, where the median disk mass is computed for each planet in a 0.1 $M_\odot$ bin around the mass of the planet's host star, including disk upper mass limits. Bottom: sum of planet masses to maximum disk mass ratio histogram and KDE, using the same binning.

4.5. Possible peas in a pod

Many works in recent years have searched for similarities between planets in multi-planet systems, a pattern that has become known as the peas in a pod scenario (e.g. Millholland et al. 2017; Hobson & Gomez 2017; Weiss et al. 2018; Otegi et al. 2022). The WG3 sample includes 21 multi-planet systems, although for some of these we have only mass upper limits, or only a lower limit of m sin i for non-transiting planets in the system. Nevertheless, we use these systems, together with a further 114 multi-planet systems from the PlanetS catalogue, to explore potential similarities between their planets. We also note the important caveat that these analyses assume no intermediate planets have been missed.

Figure 7 shows masses and radii for pairs of adjacent planets within the same system. We find that both for the WG3 sample and the PlanetS catalogue sample, the outer planets of adjacent pairs tend to be larger and more massive. For the mass, this may be a consequence of the general mass-period-metallicity relationship found by Sousa et al. (2019, 2021); alternatively, the

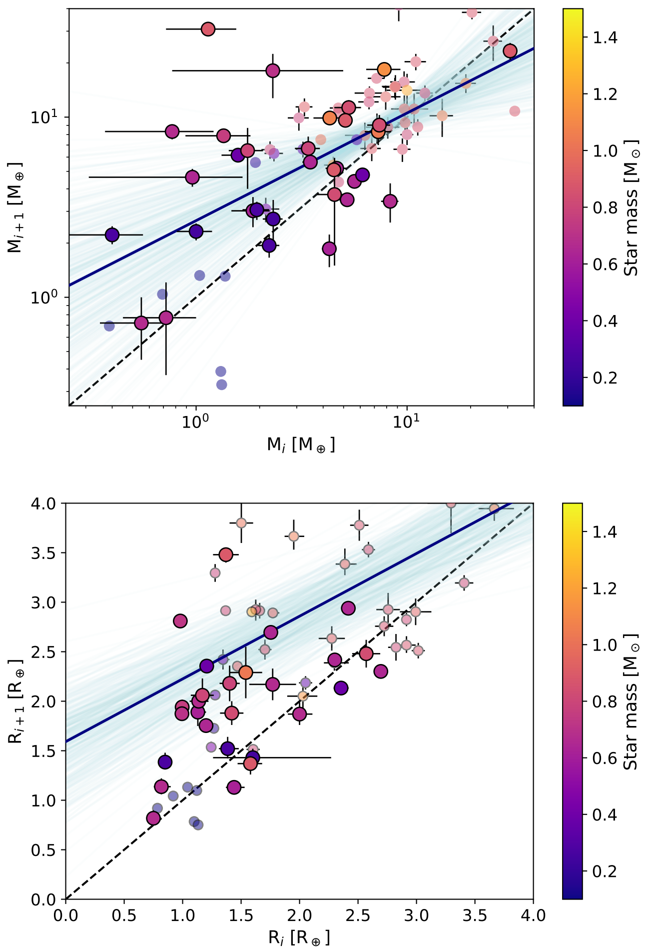

Fig. 7. Mass and radius comparison between pairs of consecutive planets. Top [Bottom]: masses [radii] of pairs of consecutive planets within a multi-planet system, for the WG3 sample (solid circles) and the PlanetS catalogue (semi-transparent circles), coloured by stellar host mass. The dashed grey line shows the 1:1 relationship. The translucent light blue lines show random draws from the `linmmix` MCMC sampling, and the solid navy line shows the median model.

period-mass part of that correlation may arise from the inclusion of systems with multiple planets. We use the `linmix` package to perform linear regression taking into account the errors, using a Gaussian mixture model and MCMC sampling. Both masses and radii may grow more similar for larger/more massive inner planets, though the dispersion in the mass fit is large.

We also find that within each system, planets tend to vary more in mass than in radius, as can be seen in Fig. 8, which plots the WG3 systems with planets coloured by mass or radius log-ratio. This is to be expected if the planets have similar densities, as $\rho \sim \frac{\mathrm{M}}{\mathrm{R}^3}$, and is further supported by a calculation of the mass and radius distance metrics, $\mathcal{D}_M = \sum_{i=1}^{N_{pl}-1} |\log \frac{M_{i+1}}{M_i}|/N_{pl}-1$ and the analogous $\mathcal{D}_R$, as defined by Otegi et al. (2022). Of the 13 WG3 systems in which we have both mass and radius for at least two planets and so can compute both metrics, 10 (77%) have larger $\mathcal{D}_M$ than $\mathcal{D}_R$. This agrees with the results of Otegi et al. (2022) on a larger sample. Likewise, we find a mean $\mathcal{D}_M/\mathcal{D}_R$ ratio of 2.8, in agreement with the observation of Otegi et al. (2022) that the values overall lie closer to the $\mathcal{D}_M = 3 \times \mathcal{D}_R$ line than the $\mathcal{D}_M = \mathcal{D}_R$ line, which they interpret as a possible correlation in density.

Regarding the planetary densities, however, which are plotted in pairs in Fig. 9, we find for both the WG3 and PlanetS samples that outer planets tend to be less dense than their adjacent inner companions. For the joint sample, we find a significant correlation (p-value = 8.7×10^{-5}). This could reflect a formation in more volatile-rich areas of the protoplanetary disk for the outer planets compared to the inner ones, potentially followed by a disk-driven migration that preserved the planet ordering. Likewise, this could also be an effect of photo-evaporation removing volatiles from the inner planets, particularly as our sample is biased towards short-period planets.

In conclusion, we find that planets orbiting low-mass stars seem to be more similar in mass, radius, and density to their system companions, compared to those orbiting higher-mass stars. This is likely due to the planets around low-mass stars having generally smaller masses and radii, while higher-mass stars host a wider range of planets.

4.6. Transmission and emission spectroscopy metrics

With the advent of the James Webb Space Telescope (JWST, Gardner et al. 2006; Rigby et al. 2023) atmospheric studies of super-Earth and sub-Neptune planets have become viable. In this section, we uniformly compute the transmission spectroscopy metric (TSM) and emission spectroscopy metric (ESM) defined by Kempton et al. (2018) for all planets discovered by the WG3, to assess their suitability for atmospheric characterisation. Figures 10 and 11 show the values obtained for TSM and ESM, respectively, for the WG3 planets, together with those from the PlanetS catalogue for comparison. Overall, most small planets with precisely measured masses and radii are not considered suitable for atmospheric characterisation by these metrics; however, around 22% fall above the TSM or ESM thresholds recommended by Kempton et al. (2018), and around 12% above both. As reliable masses are crucial to atmospheric modelling, these planets represent valuable targets for atmospheric studies.

Our survey has confirmed some highly promising planets for both transmission and emission spectroscopic characterisation, including the best TSM planets in each bin. Tables 7 and 8 list the planets above the thresholds defined by Kempton et al. (2018) for transmission and emission spectroscopy, respectively. TOI-455 c (Lavie et al. 2023, also known as LTT 1445A c) has an extremely high TSM and the second-best ESM, and is the target of an upcoming JWST Director's Discretionary Time (DDT) programme (Espinoza & Diamond-Lowe 2025), in the framework of the joint JWST/HST Rocky Worlds DDT[8], for which it was one of the first two targets announced. TOI-175 b (Demangeon et al. 2021), meanwhile, has the highest TSM for a planet with $R_p < 1.5\,R_\oplus$, and has been observed with both HST (Zhou et al. 2022) and JWST (Bello-Arufe et al. 2025), with the latter observations favouring a volcanic atmosphere.

4.7. Impact of the observing strategy

As a follow-up programme (rather than a blind survey), the WG3 observations were conducted in a way that prioritized planet confirmation. For each star, a handful of RVs were taken, from which emerging signals matching the transiting candidate period were searched for and the activity levels assessed. High-cadence RV campaigns were then performed on the most promising targets.

[8] Information available at `https://rockyworlds.stsci.edu/index.html`

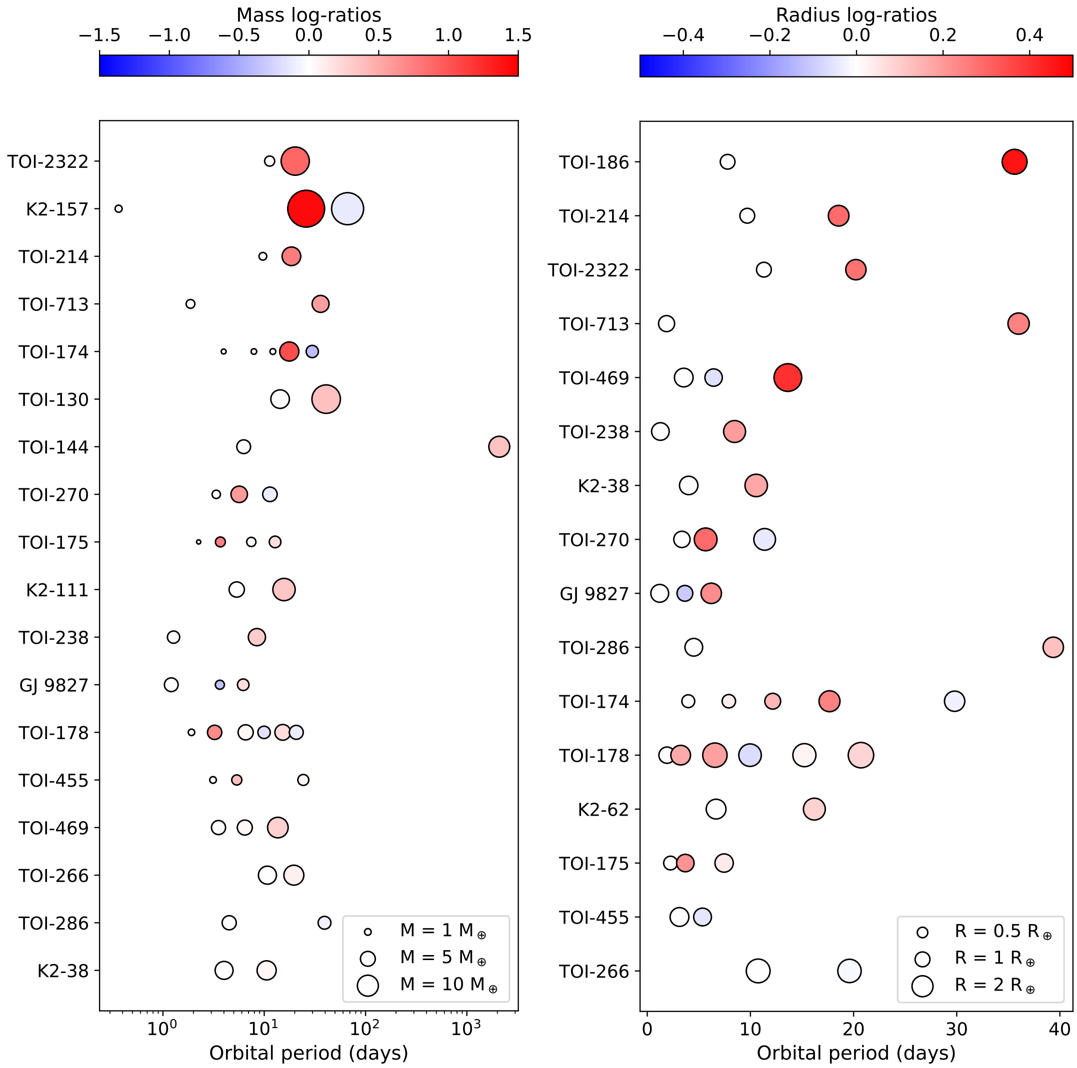

Fig. 8. Multiplanetary systems from the WG3 sample. Left (right): planets scaled by mass (radius) and coloured by mass (radius) log-ratio to the adjacent inner planet, ordered by decreasing mass (radius) distance metric as defined in Otegi et al. (2022). Note that some systems appear in only one plot, due to lack of masses or radii, and that the colour scales differ as the planets are generally more similar in radius than mass.

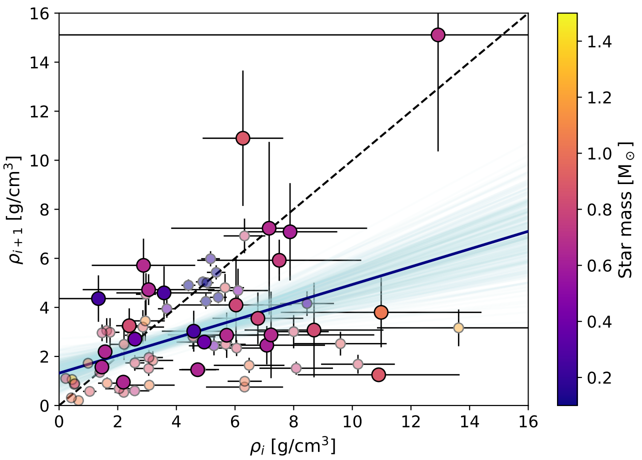

Fig. 9. Density of pairs of consecutive planets within a multi-planet system, for the WG3 sample (solid circles) and the PlanetS catalogue (semi-transparent circles), coloured by stellar host mass. The dashed grey line shows the 1:1 relationship. The translucent light blue lines show random draws from the `linmmix` MCMC sampling, and the solid navy line shows the median model.

To explore the impact of this observing strategy on the sample of confirmed planets, we plot in Fig. 12 the semi-amplitude of the planets versus the number of total RV measurements used to confirm them, showing also the ESPRESSO RV precision and ESPRESSO measurements as a percentage of the total RVs. An important result is that there appears to be a minimum threshold of ∼75 measurements required to reach semi-amplitudes significantly below the 1 m s^{-1} level. In the context of the upcoming PLATO mission, (Rauer et al. 2025, launch expected Q1 2027), which aims specifically to characterise Earth-twins for which the RV semi-amplitudes will range from ∼1 m s^{-1} for M dwarf hosts to ∼0.1 m s^{-1} for sun-like stars, this is valuable information for planning follow-up campaigns.

There is also a clear and natural tendency to prioritise targets where better RV precision can be reached, as shown by the colour scale. As the number of RV measurements increases, the error bars on the semi-amplitudes generally decrease across the left half of the figure, in line with expectations – as these targets have both more measurements and a better measurement precision – up to around 100 measurements. In the right half of the figure, however, we find some systems with hundreds of measurements and large error bars on the semi-amplitudes. This can be explained by the general decrease

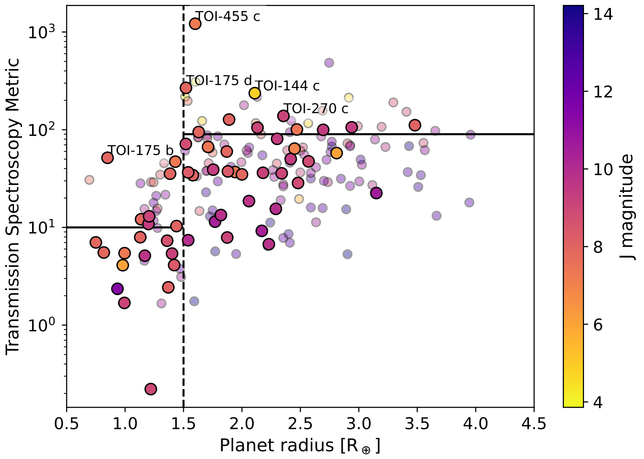

Fig. 10. TSM as a function on planet radius for the WG3-confirmed planets (solid circles), with the PlanetS catalogue planets (semi-transparent circles) included for comparison. The points are coloured by stellar J magnitude. The horizontal black lines indicate the two TSM thresholds established by Kempton et al. (2018) for planets with radii below and above 1.5R$_\oplus$, respectively, with the vertical dashed line separating the two groups.

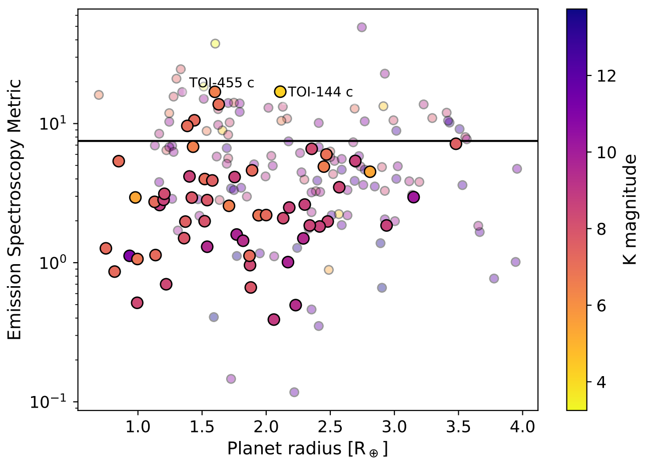

Fig. 11. ESM as a function on planet radius for the WG3-confirmed planets (solid circles), with the PlanetS catalogue planets (semi-transparent circles) included for comparison. The points are coloured by stellar K magnitude. The horizontal black line indicates the ESM threshold established by Kempton et al. (2018).

in the percentage of total RVs constituted by the ESPRESSO measurements. The inclusion of many RVs from less precise instruments, and frequently from multiple instruments with concomitant multiple inter-instrument offsets to be fitted, is then driving up the uncertainties on the semi-amplitudes.

Likewise, we see that the percentage of total RVs constituted by the ESPRESSO measurements tends to decrease with growing number of total RV measurements. Obtaining hundreds of measurements on a single target is a costly investment, that even a GTO will hesitate to make. With the smallest planets requiring large amounts of RVs for confirmation, this highlights the importance of co-operation between different surveys, as has been done, for instance, in the context of TESS follow-up. An important caveat on this is that for the smallest planets, ESPRESSO-like RV precision is necessary, which limits the co-operation possibilities.

Table 7. TSM values, planet parameters, and J magnitudes for WG3 planets above the TSM thresholds.

Name	TSM	P (d)	R_p ($R_\oplus$)	M_p ($M_\oplus$)	J mag
TOI-455 c	1215.52	3.123898	$1.60^{+0.67}_{-0.34}$	$1.00^{+0.19}_{-0.19}$	7.294
TOI-175 d	268.27	7.4507245	$1.52^{+0.12}_{-0.10}$	$1.94^{+0.28}_{-0.28}$	7.933
TOI-144 c	236.71	6.267852	$2.11^{+0.05}_{-0.05}$	$4.30^{+0.70}_{-0.70}$	4.87
TOI-270 c	138.39	5.6605731	$2.36^{+0.06}_{-0.06}$	$6.15^{+0.37}_{-0.37}$	9.099
GJ 9827 d	127.06	6.201812	$1.89^{+0.16}_{-0.14}$	$3.02^{+0.58}_{-0.57}$	7.984
TOI-469 b	111.29	13.63083	$3.48^{+0.07}_{-0.08}$	$9.60^{+0.80}_{-0.80}$	8.056
TOI-178 g	105.76	20.71663	$2.94^{+0.06}_{-0.06}$	$4.40^{+0.39}_{-0.37}$	9.372
TOI-270 d	104.92	11.379573	$2.13^{+0.06}_{-0.06}$	$4.78^{+0.43}_{-0.43}$	9.099
TOI-178 d	99.72	6.557569	$2.70^{+0.04}_{-0.05}$	$5.20^{+0.39}_{-0.43}$	9.372
TOI-134 b	94.67	1.40152604	$1.63^{+0.14}_{-0.14}$	$4.07^{+0.45}_{-0.45}$	7.941
TOI-175 b	51.61	2.2531136	$0.85^{+0.06}_{-0.05}$	$0.40^{+0.16}_{-0.15}$	7.933
TOI-455 b	47.11	5.358764	$1.43^{+0.09}_{-0.09}$	$2.32^{+0.25}_{-0.25}$	7.294
TOI-175 c	35.48	3.6906777	$1.38^{+0.10}_{-0.08}$	$2.22^{+0.26}_{-0.25}$	7.933
TOI-270 b	12.99	3.3601538	$1.21^{+0.04}_{-0.04}$	$1.58^{+0.26}_{-0.26}$	9.099
TOI-174 f	12.12	12.1621839	$1.14^{+0.08}_{-0.08}$	$0.77^{+0.44}_{-0.40}$	7.865
TOI-178 b	10.84	1.9145601	$1.20^{+0.04}_{-0.04}$	$0.96^{+0.70}_{-0.65}$	9.372
GJ 9827 b	10.32	1.208974	$1.44^{+0.09}_{-0.07}$	$4.28^{+0.35}_{-0.33}$	7.984

Notes. Top: planets with $R_p \geq 1.5\,R_\oplus$. Bottom: planets with $R_p < 1.5\,R_\oplus$.

Table 8. ESM values, planet parameters, and K magnitude for WG3 planets above the ESM threshold.

Name	ESM	P (d)	R_p ($R_\oplus$)	M_p ($M_\oplus$)	K mag
TOI-144 c	16.95	6.267852	$2.11^{+0.05}_{-0.05}$	$4.30^{+0.70}_{-0.70}$	4.241
TOI-455 c	16.91	3.123898	$1.60^{+0.67}_{-0.34}$	$1.00^{+0.19}_{-0.19}$	6.496
TOI-134 b	13.75	1.40152604	$1.63^{+0.14}_{-0.14}$	$4.07^{+0.45}_{-0.45}$	7.082
GJ 9827 b	10.56	1.208974	$1.44^{+0.09}_{-0.07}$	$4.28^{+0.35}_{-0.33}$	7.193
TOI-175 c	9.62	3.6906777	$1.38^{+0.10}_{-0.08}$	$2.22^{+0.26}_{-0.25}$	7.101

4.8. Stellar activity characterisation

Stellar activity is a well-known confounding factor in exoplanet RV surveys, with active regions on the stellar surface producing spurious RV signals that can mimic or mask true planetary signals (e.g. Dumusque et al. 2014; Dumusque 2018, and references therein). Transit follow-up surveys are privileged in this regard, as the additional transit information can enable the separation of planetary and activity signals even when the periods are similar. This has been crucial to the analysis of three systems from the WG3 (Hobson et al. 2024, 2025, ; Barros et al., in prep).

The ESPRESSO pipeline provides numerous activity indicators, as described in Sect. 3.1.1. The question then arises regarding which indicators are the most effective for our sample. To study this, we selected the WG3 targets with at least fifty observations to allow for a sufficient number of data points for quasi-periodic activity signals to emerge clearly. This sample consists of 18 stars. For these stars, we generated periodograms of all the activity indicators, and inspected the periodograms for significant signals. For each star, we recorded the indicator with the lowest FAP, as a proxy for the most effective indicator.

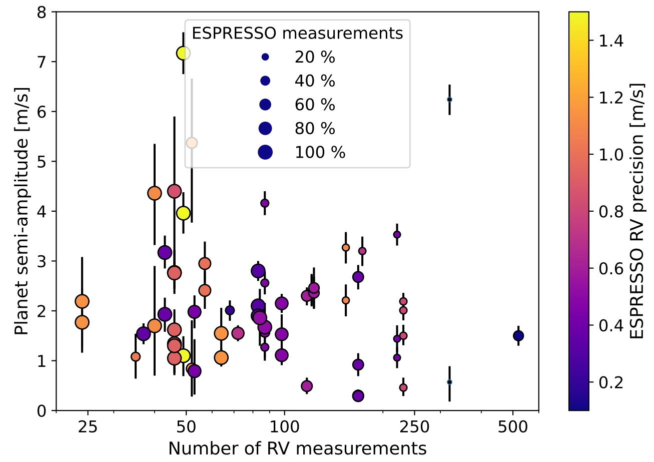

Fig. 12. Semi-amplitude of the WG3 planets versus number of RV measurements used to confirm them. The points are coloured by the ESPRESSO RV precision and scaled by the percentage of ESPRESSO measurements.

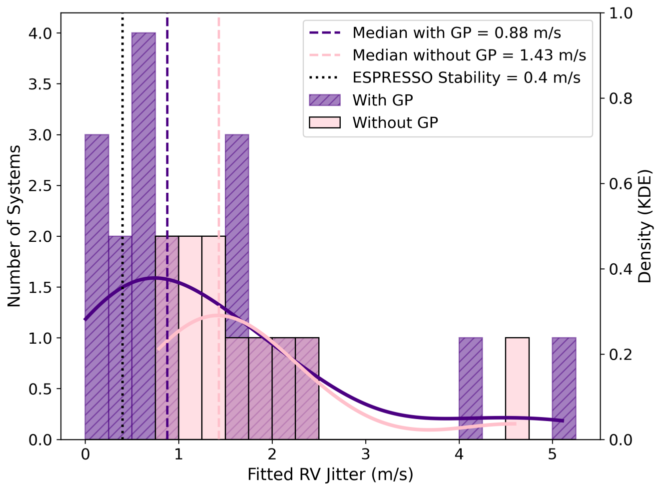

Fig. 13. Histograms and KDEs (solid lines) of the fitted RV jitter for the WG3 systems that were modelled without additional GP activity modelling (semi-transparent pink), and with GP modelling (semi-transparent hatched purple). The dashed vertical pink and purple lines show the median RV jitter for systems without and with GP modelling, respectively. The dotted black line shows ESPRESSO's long-term RV-precision.

For just over half the sample (10 targets) the FWHM proved to be the most effective indicator, with the remainder being fairly evenly distributed among the other indicators. This is consistent with previous findings on Proxima Centauri Faria et al. (2022), which was intensively observed in the blind survey GTO sub-programme, and for which the FWHM shows the strongest activity signals. We also compared the signals seen in the activity indicators to predicted rotation periods using the $\log R'_{\rm hk}$-P_{rot} relation from Suárez Mascareño et al. (2015). We find an overall good agreement between the predicted rotation periods and the strongest signals in the activity indicator periodograms, though for some targets the first harmonic of the predicted rotation period shows more power than the expected rotation period itself. This has previously been observed in both simulations (Boisse et al. 2011) and HARPS observational data (Suárez Mascareño et al. 2017), and is dependent on the configuration of the active regions and the inclination of the stellar axis.

Another way to look at the impact of stellar activity on our survey is to examine the fitted RV jitter. This is a white noise term typically included in RV modelling to account for residual stellar effects such as oscillation and granulation noise, instrumental effects, and unmodelled planets. The RV jitter for each of the systems characterised by the WG3 is listed in Table 3. To study this jitter, we divide the systems into two groups: those where a GP was used to model the stellar activity, which should reduce the amount of residual activity-induced RV variation (18 systems); and those without activity modelling (11 systems). Figure 13 shows the RV jitter distributions for each group. It is clear that adding a GP model tends to result in a substantial decrease of the fitted RV jitter, as expected. However, given ESPRESSO's excellent long-term RV stability of 40 cm s^{-1} compared to the median RV jitter of 88 cm s^{-1} for models including a GP, it is apparent that there is still stellar-activity-induced RV variation that remains unaccounted for, even after GP modelling. Stellar activity is thus clearly the greatest current obstacle to detecting and characterising the smallest planets.

5. Conclusions

We present an overview of the WG3 sub-programme of the ESPRESSO GTO, dedicated to the follow-up, confirmation, and characterisation of small transiting planets from K2 and TESS. We studied the sample of characterised planets, placing them in the context of the overall planet population. Our main results are:

- In the 50–200 $S_\oplus$ insolation range, there is a tentative rocky-to-volatile transition threshold mass at ~6 $M_\oplus$, with planets below this mass being rocky and planets above this mass being volatile-rich;
- In the high-insolation regime, we find a population of high-mass rocky planets (~6–10 $M_\oplus$) that are not observed at lower insolations, suggesting these planets are stripped cores;
- Planets below the radius valley have a narrow mass distribution with a sharp cut-off at ~10$M_\oplus$, while planets above the valley have a broad distribution spanning the full mass range. The mass distributions intersect at ~6 $M_\oplus$, in line with the proposed rocky-to-volatile threshold;
- Planetary mass is correlated with metallicity and we find more massive planets around more metal-rich stars;
- Planetary masses are comparable to the median protoplanetary disk mass in their stellar mass range, suggesting these rocky planets form either in massive disks, with a high formation efficiency, or very early in the disk's lifetime;
- In multiplanetary systems, outer planets tend to be more massive, bigger, and less dense than inner ones;
- The ESPRESSO WG3 sub-programme provides many valuable targets for atmospheric characterisation;
- The results from our observing strategy can serve as a guide for the follow-up for the upcoming PLATO mission. Generally, at least ≈ 75 measurements are required for measuring semi-amplitudes below the ≈50 cm s^{-1} level;
- For ESPRESSO data, the FWHM is generally the most reliable activity indicator. The fitted residual RV jitter suggests that even with activity modelling via GPs, there is significant uncharacterised RV noise induced by stellar activity that remains to be explored.

Acknowledgements. We thank the Swiss National Science Foundation (SNSF) and the Geneva University for their continuous support to our planet low-mass companion search programmes. This work has been carried out within the framework of the National Centre of Competence in Research PlanetS supported by the Swiss National Science Foundation under grants 51NF40_182901 and 51NF40_205606. The authors acknowledge the financial support of the SNSF. This publication makes use of The Data & Analysis Center for Exoplanets (DACE), which is a facility based at the University of Geneva (CH) dedicated to extrasolar planets data visualisation, exchange and analysis. DACE is a platform of the Swiss National Centre of Competence in Research (NCCR) PlanetS, federating the Swiss expertise in Exoplanet research. The DACE platform is available at https://dace.unige.ch. Funding for the TESS mission is provided by NASA's Science Mission Directorate. This paper made use of data collected by the TESS mission and are publicly available from the Mikulski Archive for Space Telescopes (MAST) operated by the Space Telescope Science Institute (STScI). We acknowledge the use of public TESS data from pipelines at the TESS Science Office and at the TESS Science Processing Operations Center. Resources supporting this work were provided by the NASA High-End Computing (HEC) Program through the NASA Advanced Supercomputing (NAS) Division at Ames Research Center for the production of the SPOC data products. Based on observations collected at the European Southern Observatory under ESO programmes 0102.C-0456, 106.21M2, 108.2254, 110.24CD, 1102.C-0744, 1102.C-0958, 1104.C-0350, and 112.25BG. This research made use of Lightkurve, a Python package for Kepler and TESS data analysis (Lightkurve Collaboration 2018). JIGH, ASM, CAP and RR acknowledge financial support from the Spanish Ministry of Science, Innovation and Universities (MICIU) project PID2023-149982NB-I00. Funded/Co-funded by the European Union (ERC, FIERCE, 101052347). Views and opinions expressed are however those of the author(s) only and do not necessarily reflect those of the European Union or the European Research Council. Neither the European Union nor the granting authority can be held responsible for them. This work was supported by FCT – Fundação para a Ciência e a Tecnologia through national funds by grants reference UID/04434/2025. X.D. acknowledges the support from the the Swiss National Science Foundation under the grant SPECTRE (No. 200021_215200). This work was financed by Portuguese funds through FCT (Fundação para a Ciência e a Tecnologia) in the framework of the project 2022.04048.PTDC (Phi in the Sky, DOI 10.54499/2022.04048.PTDC). CJM also acknowledges FCT and POCH/FSE (EC) support through Investigador FCT Contract 2021.01214.CEECIND/CP1658/CT0001 (DOI 10.54499/2021.01214.CEECIND/CP1658/CT0001). A.S.M. acknowledges financial support from the Spanish Ministry of Science and Innovation (MICINN) project PID2020-117493GB-I00. S.G.S. acknowledges support from FCT through FCT contract nr. CEECIND/00826/2018 and POPH/FSE (EC). We acknowledge financial support from the Agencia Estatal de Investigación of the Ministerio de Ciencia e Innovación MCIN/AEI/10.13039/501100011033 and the ERDF "A way of making Europe" through projects PID2021-125627OB-C32 and PID2024-158486OB-C32. This work was financed by FCT – Fundação para a Ciência e a Tecnologia under projects UIDB/04434/2020 DOI:10.54499/UIDB/04434/2020, UIDP/04434/2020 DOI: 10.54499/UIDP/04434/2020, PTDC/FIS-AST/4862/2020, UID/04434/2025. J.L.-B. is funded by the Spanish grants PID2023-150468NB-I00 and CNS2023-144309 from the Ministry of Science, Innovation and Universities (MCIN/AEI/10.13039/501100011033). Pedro Figueira acknowledges financial support from the Severo Ochoa grant CEX2021-001131-S funded by MCIN/AEI/10.13039/501100011033. Pedro Figueira is also funded by the European Union (ERC, THIRSTEE, 101164189). Views and opinions expressed are however those of the author(s) only and do not necessarily reflect those of the European Union or the European Research Council. Neither the European Union nor the granting authority can be held responsible for them. O.D.S.D. acknowledges support from e-CHEOPS (PEA No 4000142255).

References

Akana Murphy, J. M., Batalha, N. M., Scarsdale, N., et al. 2023, AJ, 166, 153
Ambikasaran, S., Foreman-Mackey, D., Greengard, L., Hogg, D. W., & O'Neil, M. 2015, IEEE Trans. Pattern Anal. Mach. Intell., 38, 252
Antoniadis-Karnavas, A., Sousa, S. G., Delgado-Mena, E., et al. 2020, A&A, 636, A9
Armstrong, D. J., Lopez, T. A., Adibekyan, V., et al. 2020, Nature, 583, 39
Armstrong, D. J., Osborn, A., Burn, R., et al. 2025, MNRAS, 537, 3175
Astropy Collaboration (Price-Whelan, A. M., et al.) 2022, ApJ, 935, 167
Baranne, A., Queloz, D., Mayor, M., et al. 1996, A&AS, 119, 373
Barros, S. C. C., Demangeon, O. D. S., Alibert, Y., et al. 2022, A&A, 665, A154
Baumeister, P., & Tosi, N. 2023, A&A, 676, A106
Bean, J. L., Raymond, S. N., & Owen, J. E. 2021, J. Geophys. Res. (Planets), 126, e06639
Bello-Arufe, A., Damiano, M., Bennett, K. A., et al. 2025, ApJ, 980, L26
Boisse, I., Bouchy, F., Hébrard, G., et al. 2011, A&A, 528, A4
Boley, K. M., Christiansen, J. L., Zink, J., et al. 2024, AJ, 168, 128
Bonfils, X., Mayor, M., Delfosse, X., et al. 2007, A&A, 474, 293
Borucki, W. J., Koch, D., Basri, G., et al. 2010, Science, 327, 977
Brahm, R., Espinoza, N., Jordán, A., et al. 2019, AJ, 158, 45
Bressan, A., Marigo, P., Girardi, L., et al. 2012, MNRAS, 427, 127
Burn, R., Mordasini, C., Mishra, L., et al. 2024, arXiv e-prints [arXiv:2401.04380]
Castro-González, A., Díez Alonso, E., Menéndez Blanco, J., et al. 2022, MNRAS, 509, 1075
Castro-González, A., Demangeon, O. D. S., Lillo-Box, J., et al. 2023, A&A, 675, A52
Castro-González, A., Bouchy, F., Correia, A. C. M., et al. 2025, A&A, 699, A344
Chen, D.-C., Mordasini, C., Emsenhuber, A., et al. 2025, A&A, 701, A94
Cincunegui, C., Díaz, R. F., & Mauas, P. J. D. 2007, A&A, 469, 309
Courcol, B., Bouchy, F., & Deleuil, M. 2016, MNRAS, 461, 1841
Crane, J. D., Shectman, S. A., Butler, R. P., et al. 2010, SPIE Conf. Ser., 7735, 773553
Damasso, M., Sozzetti, A., Lovis, C., et al. 2020, A&A, 642, A31
Damasso, M., Rodrigues, J., Castro-González, A., et al. 2023, A&A, 679, A33
Demangeon, O. D. S., Zapatero Osorio, M. R., Alibert, Y., et al. 2021, A&A, 653, A41
Díaz, R. F., Cincunegui, C., & Mauas, P. J. D. 2007, MNRAS, 378, 1007
Dragomir, D., Teske, J., Günther, M. N., et al. 2019, ApJ, 875, L7
Dumusque, X. 2018, A&A, 620, A47
Dumusque, X., Boisse, I., & Santos, N. C. 2014, ApJ, 796, 132
Eastman, J., Gaudi, B. S., & Agol, E. 2013, PASP, 125, 83
Espinoza, N., & Diamond-Lowe, H. 2025, Rocky Worlds DDT: JWST Observations of LTT 1445 A c, JWST Proposal. Cycle 3, ID. #9234
Espinoza, N., Brahm, R., Jordán, A., et al. 2016, ApJ, 830, 43
Espinoza, N., Kossakowski, D., & Brahm, R. 2019, MNRAS, 490, 2262
Faria, J. P., Suárez Mascareño, A., Figueira, P., et al. 2022, A&A, 658, A115
Fatuzzo, M., & Adams, F. C. 2008, ApJ, 675, 1361
Figueira, P., Faria, J. P., Silva, A. M., et al. 2025, A&A, 700, A174
Foreman-Mackey, D., Agol, E., Ambikasaran, S., & Angus, R. 2017, AJ, 154, 220
Fortney, J. J., Marley, M. S., & Barnes, J. W. 2007, ApJ, 659, 1661
Fressin, F., Torres, G., Charbonneau, D., et al. 2013, ApJ, 766, 81
Fulton, B. J., Petigura, E. A., Howard, A. W., et al. 2017, AJ, 154, 109
Fulton, B. J., Petigura, E. A., Blunt, S., & Sinukoff, E. 2018, PASP, 130, 044504
Gaia Collaboration (Prusti, T., et al.) 2016, A&A, 595, A1
Gaia Collaboration (Vallenari, A., et al.) 2023, A&A, 674, A1
Gardner, J. P., Mather, J. C., Clampin, M., et al. 2006, Space Sci. Rev., 123, 485
Ginsburg, A., Sipőcz, B. M., Brasseur, C. E., et al. 2019, AJ, 157, 98
Gonzalez, G. 1997, MNRAS, 285, 403
Guerrero, N. M., Seager, S., Huang, C. X., et al. 2021, ApJS, 254, 39
Haworth, T. J., Clarke, C. J., Rahman, W., Winter, A. J., & Facchini, S. 2018, MNRAS, 481, 452
Haworth, T. J., Coleman, G. A. L., Qiao, L., Sellek, A. D., & Askari, K. 2023, MNRAS, 526, 4315
Haywood, R. D., Collier Cameron, A., Queloz, D., et al. 2014, MNRAS, 443, 2517
Heller, R., & Armstrong, J. 2014, Astrobiology, 14, 50
Ho, C. S. K., & Van Eylen, V. 2023, MNRAS, 519, 4056
Hobson, M. J., & Gomez, M. 2017, New A, 55, 1
Hobson, M. J., Bouchy, F., Lavie, B., et al. 2024, A&A, 688, A216
Hobson, M. J., Suárez Mascareño, A., Lovis, C., et al. 2025, A&A, 702, A32
Høg, E., Fabricius, C., Makarov, V. V., et al. 2000, A&A, 355, L27
Howell, S. B., Sobeck, C., Haas, M., et al. 2014, PASP, 126, 398
Ida, S., & Lin, D. N. C. 2004, ApJ, 616, 567
Jao, W.-C., Henry, T. J., Subasavage, J. P., et al. 2011, AJ, 141, 117
Jenkins, J. M. 2002, ApJ, 575, 493
Jenkins, J. M., Chandrasekaran, H., McCauliff, S. D., et al. 2010, SPIE Conf. Ser., 7740, 77400D
Jenkins, J. M., Twicken, J. D., McCauliff, S., et al. 2016, SPIE Conf. Ser., 9913, 99133E
Jenkins, J. M., Tenenbaum, P., Seader, S., et al. 2020, Kepler Data Processing Handbook: Transiting Planet Search, Kepler Science Document KSCI-19081-003
Kar, A., Henry, T. J., Couperus, A. A., Vrijmoet, E. H., & Jao, W.-C. 2024, AJ, 167, 196
Kelly, B. C. 2007, ApJ, 665, 1489
Kempton, E. M. R., Bean, J. L., Louie, D. R., et al. 2018, PASP, 130, 114401
Kipping, D. M. 2013, MNRAS, 435, 2152
Koen, C., Kilkenny, D., van Wyk, F., & Marang, F. 2010, MNRAS, 403, 1949
Kreidberg, L. 2015, PASP, 127, 1161
Lada, C. J., & Lada, E. A. 2003, ARA&A, 41, 57
Lavie, B., Bouchy, F., Lovis, C., et al. 2023, A&A, 673, A69
Leleu, A., Alibert, Y., Hara, N. C., et al. 2021, A&A, 649, A26
Leleu, A., Delisle, J.-B., Delrez, L., et al. 2024, A&A, 688, A211

Lightkurve Collaboration (Cardoso, J. V. d. M., et al.) 2018, Lightkurve: Kepler and TESS time series analysis in Python, Astrophysics Source Code Library [record ascl:1812.013]
Livingston, J. H., Crossfield, I. J. M., Petigura, E. A., et al. 2018, AJ, 156, 277
Luo, H., Dorn, C., & Deng, J. 2024, Nat. Astron., 8, 1399
Luque, R., & Pallé, E. 2022, Science, 377, 1211
Manara, C. F., Ansdell, M., Rosotti, G. P., et al. 2023, in Astronomical Society of the Pacific Conference Series, 534, Protostars and Planets VII, eds. S. Inutsuka, Y. Aikawa, T. Muto, K. Tomida, & M. Tamura, 539
Mayo, A. W., Vanderburg, A., Latham, D. W., et al. 2018, AJ, 155, 136
Mayor, M., Pepe, F., Queloz, D., et al. 2003, The Messenger, 114, 20
Mayor, M., Marmier, M., Lovis, C., et al. 2011, arXiv e-prints [arXiv:1109.2497]
Millholland, S., Wang, S., & Laughlin, G. 2017, ApJ, 849, L33
Mortier, A., Santos, N. C., Sozzetti, A., et al. 2012, A&A, 543, A45
Mortier, A., Zapatero Osorio, M. R., Malavolta, L., et al. 2020, MNRAS, 499, 5004
Mulders, G. D., Pascucci, I., Ciesla, F. J., & Fernandes, R. B. 2021, ApJ, 920, 66
Murgas, F., Pallé, E., Suárez Mascareño, A., et al. 2025, A&A, 703, A201
Narita, N., Hirano, T., Fukui, A., et al. 2017, PASJ, 69, 29
Noyes, R. W., Hartmann, L. W., Baliunas, S. L., Duncan, D. K., & Vaughan, A. H. 1984, ApJ, 279, 763
Otegi, J. F., Bouchy, F., & Helled, R. 2020, A&A, 634, A43
Otegi, J. F., Helled, R., & Bouchy, F. 2022, A&A, 658, A107
Parc, L., Bouchy, F., Venturini, J., Dorn, C., & Helled, R. 2024, A&A, 688, A59
Passegger, V. M., Suárez Mascareño, A., Allart, R., et al. 2024, A&A, 684, A22
Patel, J. A., & Espinoza, N. 2022, AJ, 163, 228
Pecaut, M. J., & Mamajek, E. E. 2013, ApJS, 208, 9
Pepe, F., Cristiani, S., Rebolo, R., et al. 2013, The Messenger, 153, 6
Pepe, F., Cristiani, S., Rebolo, R., et al. 2021, A&A, 645, A96
Petigura, E. A., Rogers, J. G., Isaacson, H., et al. 2022, AJ, 163, 179
Qiao, L., Coleman, G. A. L., & Haworth, T. J. 2026, MNRAS, 546, stag034
Queloz, D., Henry, G. W., Sivan, J. P., et al. 2001, A&A, 379, 279
Rauer, H., Aerts, C., Cabrera, J., et al. 2025, Exp. Astron., 59, 26
Ricker, G. R., Winn, J. N., Vanderspek, R., et al. 2015, J. Astron. Telesc. Instrum. Syst., 1, 014003
Rigby, J., Perrin, M., McElwain, M., et al. 2023, PASP, 135, 048001
Rodrigues, J., Barros, S. C. C., Santos, N. C., et al. 2025, A&A, 695, A237
Rogers, L. A. 2015, ApJ, 801, 41
Santos, N. C., Israelian, G., & Mayor, M. 2001, A&A, 373, 1019
Santos, N. C., Sousa, S. G., Mortier, A., et al. 2013, A&A, 556, A150
Scally, A., & Clarke, C. 2001, MNRAS, 325, 449
Skrutskie, M. F., Cutri, R. M., Stiening, R., et al. 2006, AJ, 131, 1163
Smith, J. C., Stumpe, M. C., Van Cleve, J. E., et al. 2012, PASP, 124, 1000
Sousa, S. G. 2014, in Determination of Atmospheric Parameters of B, 297
Sousa, S. G., Adibekyan, V., Santos, N. C., et al. 2019, MNRAS, 485, 3981
Sousa, S. G., Adibekyan, V., Delgado-Mena, E., et al. 2021, A&A, 656, A53
Sozzetti, A., Damasso, M., Bonomo, A. S., et al. 2021, A&A, 648, A75
Speagle, J. S. 2020, MNRAS, 493, 3132
Stassun, K. G. 2019, VizieR Online Data Catalog, IV/38
Störzer, H., & Hollenbach, D. 1999, ApJ, 515, 669
Stumpe, M. C., Smith, J. C., Van Cleve, J. E., et al. 2012, PASP, 124, 985
Stumpe, M. C., Smith, J. C., Catanzarite, J. H., et al. 2014, PASP, 126, 100
Suárez Mascareño, A., Passegger, V. M., González Hernández, J. I., et al. 2024, A&A, 685, A56
Suárez Mascareño, A., Rebolo, R., González Hernández, J. I., & Esposito, M. 2015, MNRAS, 452, 2745
Suárez Mascareño, A., Rebolo, R., González Hernández, J. I., & Esposito, M. 2017, MNRAS, 468, 4772
Tabernero, H. M., Marfil, E., Montes, D., & González Hernández, J. I. 2022, A&A, 657, A66
Tayar, J., Claytor, Z. R., Huber, D., & van Saders, J. 2022, ApJ, 927, 31
Toledo-Padrón, B., Lovis, C., Suárez Mascareño, A., et al. 2020, A&A, 641, A92
Trifonov, T., Rybizki, J., & Kürster, M. 2019, A&A, 622, L7
Tychoniec, Ł., Manara, C. F., Rosotti, G. P., et al. 2020, A&A, 640, A19
Udry, S., & Santos, N. C. 2007, ARA&A, 45, 397
Valencia, D., Sasselov, D. D., & O'Connell, R. J. 2007, ApJ, 656, 545
Van Eylen, V., Agentoft, C., Lundkvist, M. S., et al. 2018, MNRAS, 479, 4786
Van Eylen, V., Astudillo-Defru, N., Bonfils, X., et al. 2021, MNRAS, 507, 2154
Vaughan, A. H., Preston, G. W., & Wilson, O. C. 1978, PASP, 90, 267
Venturini, J., Guilera, O. M., Haldemann, J., Ronco, M. P., & Mordasini, C. 2020, A&A, 643, L1
Venturini, J., Ronco, M. P., Guilera, O. M., et al. 2024, A&A, 686, L9
Virtanen, P., Gommers, R., Oliphant, T. E., et al. 2020, Nat. Methods, 17, 261
Vogt, S. S., Allen, S. L., Bigelow, B. C., et al. 1994, SPIE Conf. Ser., 2198, 362
Weiss, L. M., Marcy, G. W., Petigura, E. A., et al. 2018, AJ, 155, 48
Wenger, M., Ochsenbein, F., Egret, D., et al. 2000, A&AS, 143, 9
Winter, A. J., & Haworth, T. J. 2022, Eur. Phys. J. Plus, 137, 1132
Zacharias, N., Finch, C. T., Girard, T. M., et al. 2013, AJ, 145, 44
Zapatero Osorio, M. R., Tabernero, H., Suárez Mascareño, A., et al. 2026, A&A, 706, A166
Zeng, L., Jacobsen, S. B., Sasselov, D. D., et al. 2019, PNAS, 116, 9723
Zhou, L., Ma, B., Wang, Y., & Zhu, Y. 2022, AJ, 164, 203
Zhu, W., Dong, S. 2021, ARA&A, 59, 291

---

[1] Observatoire de Genève, Département d'Astronomie, Université de Genève, Chemin Pegasi 51b, 1290 Versoix, Switzerland
[2] Instituto de Astrofísica e Ciências do Espaço, CAUP, Universidade do Porto, Rua das Estrelas, 4150-762 Porto, Portugal
[3] Departamento de Física e Astronomia, Faculdade de Ciências, Universidade do Porto, Rua do Campo Alegre, 4169-007 Porto, Portugal
[4] Institut d'Estudis Espacials de Catalunya (IEEC), Edifici RDIT, Campus UPC, 08860 Castelldefels (Barcelona), Spain
[5] Institut de Ciències de l'Espai (ICE, CSIC), Campus UAB, c/ de Can Magrans s/n, 08193 Cerdanyola del Vallès, Barcelona, Spain
[6] Space Research Institute, Austrian Academy of Sciences, Schmiedlstrasse 6, 8042 Graz, Austria
[7] Institute of Astronomy, KU Leuven, Celestijnlaan 200D, 3001 Leuven, Belgium
[8] University of Geneva, Faculty of Science, Geneva, Switzerland
[9] Instituto de Astrofísica de Canarias, c/ Vía Láctea s/n, 38205 La Laguna, Tenerife, Spain
[10] Departamento de Astrofísica, Universidad de La Laguna, 38206 La Laguna, Tenerife, Spain
[11] Physics Institute, University of Bern, Gesellsschaftstrasse 6, 3012 Bern, Switzerland
[12] Center for Space and Habitability, University of Bern, Gesellschaftstrasse 6, 3012 Bern, Switzerland
[13] INAF– Osservatorio Astronomico di Trieste, via G. B. Tiepolo 11, 34143 Trieste, Italy
[14] IFPU–Institute for Fundamental Physics of the Universe, via Beirut 2, 34151 Trieste, Italy
[15] Instituto de Astrofísica de Andalucía-CSIC, Glorieta de la Astronomía s/n, 18008 Granada, Spain
[16] Centro de Astrobiología, CSIC-INTA, Camino Bajo del Castillo s/n, 28692 Villanueva de la Cañada, Madrid, Spain
[17] European Southern Observatory, Av. Alonso de Cordova, 3107, Vitacura, Santiago de Chile, Chile
[18] Centro de Astrofísica da Universidade do Porto, Rua das Estrelas, 4150-762 Porto, Portugal
[19] INAF – Osservatorio Astronomico di Palermo, Piazza del Parlamento 1, 90134, Palermo, Italy
[20] Instituto de Astrofísica e Ciências do Espaço, Faculdade de Ciências da Universidade de Lisboa, 1749-016 Lisboa, Portugal
[21] Consejo Superior de Investigaciones Científicas, 28006 Madrid, Spain
[22] INAF – Osservatorio Astrofisico di Torino, Via Osservatorio 20, 10025 Pino Torinese, Italy

Appendix A: Stellar parameters for stars with few spectra

In this appendix, we present the atmospheric stellar parameters for WG3 targets with fewer than ten ESPRESSO spectra.

Table A.1. Stellar parameters for WG3 targets with fewer than ten spectra.

Name	V [mag][a]	$T_{\rm eff}$ [K]	Fe/H [dex]	$\log g$ [dex]	$V_{\rm broad}$ [km s^{-1}]
TOI-1203	8.59†	5617 ± 113	4.1 ± 0.02	−0.53 ± 0.02	1.55 ± 0.03
TOI-1233	9.24†	5707 ± 115	4.49 ± 0.02	−0.33 ± 0.01	1.58 ± 0.01
TOI-696	12.482⋆	3536 ± 73	4.81 ± 0.08	−0.5 ± 0.04	≤ 1.0
K2-155	12.806⋆	4173 ± 89	4.13 ± 0.12	−0.73 ± 0.04	1.4 ± 0.05
TOI-438	10.24†	5186 ± 105	4.47 ± 0.03	0.04 ± 0.01	1.42 ± 0.02
TOI-1130	11.59†	4436 ± 89	4.72 ± 0.02	−0.04 ± 0.01	1.45 ± 0.02
TOI-871	10.57†	4975 ± 101	4.49 ± 0.04	−0.15 ± 0.01	1.29 ± 0.03
TOI-1063	9.80†	5295 ± 107	4.74 ± 0.02	−0.04 ± 0.01	2.73 ± 0.04
TOI-1078	12.20♯	3474 ± 73	4.87 ± 0.05	−0.17 ± 0.06	2.0 ± 0.04
TOI-704	12.00†	3599 ± 74	4.54 ± 0.07	−0.28 ± 0.05	2.21 ± 0.04
TOI-1097	9.31†	5941 ± 120	4.62 ± 0.03	0.0 ± 0.04	5.13 ± 0.03
TOI-1230	10.25†	5910 ± 120	4.68 ± 0.04	−0.43 ± 0.03	1.78 ± 0.02
TOI-1468	13.124⋆	3438 ± 69	4.69 ± 0.05	−0.19 ± 0.05	2.05 ± 0.08
TOI-1058	10.81†	5834 ± 122	3.71 ± 0.06	0.0 ± 0.02	4.74 ± 0.05
TOI-910	12.69◊	3401 ± 72	4.85 ± 0.08	−0.12 ± 0.07	2.11 ± 0.05

Notes. [a]: V magnitude sources: †: the Tycho-2 Catalogue (Høg et al. 2000), ⋆: The Fourth US Naval Observatory CCD Astrograph Catalog (UCAC4, Zacharias et al. 2013), ♯: Kar et al. (2024), ◊: Jao et al. (2011).

Appendix B: Juliet fit parameters and plots

In this appendix, we present the fitted and derived parameters for the `juliet` fits described in Section 3.3. We also present the RV and photometric plots.

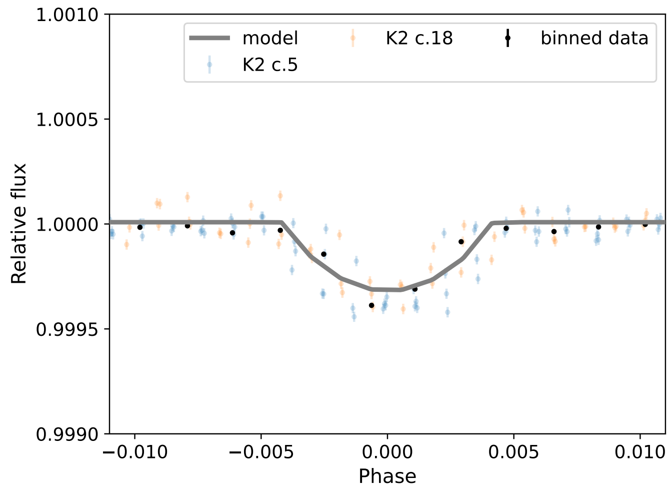

Fig. B.1. Phase-folded K2 data with the median 1*e_gp* model (grey line) for K2-184 b. The points show the data from K2 campaign 5 (blue), K2 campaign 18 (orange), and binned data (black).

Table B.1. Prior and posterior planetary parameter distributions obtained with `juliet` for K2-184, for the 1*e_gp* model.

Parameter	Prior	Posterior
$\mu_{\rm ESPRESSO18}$ [m s^{-1}]	$\mathcal{U}(-33353.8, -33335.1)$	-33344.0 ± 1.6
$\sigma_{\rm w,ESPRESSO18}$ [m s^{-1}]	$\mathcal{J}(0.001, 10)$	$2.47^{+0.45}_{-0.38}$
$\mu_{\rm ESPRESSO19}$ [m s^{-1}]	$\mathcal{U}(-33347.8, -33333.0)$	$-33342.5^{+1.6}_{-1.9}$
$\sigma_{\rm w,ESPRESSO19}$ [m s^{-1}]	$\mathcal{J}(0.001, 10)$	$0.11^{+1.23}_{-0.10}$
P_1 . . . . [d]	$\mathcal{N}(16.978, 0.001)$	$16.977959^{+0.000089}_{-0.000090}$
$t_{0,1}$ . . . . . [BJD]	$\mathcal{N}(2457148.53, 0.01)$	$2457148.5219^{+0.0023}_{-0.0020}$
$\sqrt{e}\sin\omega_1$	$\mathcal{U}(-1, 1)$	$0.02^{+0.34}_{-0.30}$
$\sqrt{e}\cos\omega_1$	$\mathcal{U}(-1, 1)$	$-0.71^{+0.14}_{-0.05}$
K_1	$\mathcal{U}(0, 10)$	$4.4^{+1.5}_{-1.6}$
ρ . . . . [kg m^{-3}]	$\mathcal{J}(100, 10000)$	$1748.3^{+1811.5}_{-967.5}$
p_1	$\mathcal{N}(0.02, 0.1)$	$0.01467^{+0.00074}_{-0.00068}$
b_1	$\mathcal{N}(0.42, 0.1)$	$0.407^{+0.093}_{-0.088}$
$q1_{\rm K2-5,K2-18}$ . . .	$\mathcal{U}(0, 1)$	$0.896^{+0.071}_{-0.106}$
$q2_{\rm K2-5,K2-18}$ . . .	$\mathcal{U}(0, 1)$	$0.930^{+0.050}_{-0.078}$
$\sigma_{\rm GP,rv}$	$\mathcal{TN}(11.1, 7.8, 0, 1000)$	$4.1^{+1.0}_{-0.8}$
$\alpha_{\rm GP,rv}$	$\mathcal{TN}(0.008, 0.029, 0, 1000)$	$0.026^{+0.023}_{-0.017}$
$\Gamma_{\rm GP,rv}$	$\mathcal{TN}(2.1, 4.0, 0, 1000)$	$5.2^{+3.1}_{-2.4}$
${\rm Prot}_{\rm GP,rv}$	$\mathcal{N}(53.1, 22.1)$	$47.9^{+19.9}_{-17.3}$
$m_{\rm flux,K2-5}$	$\mathcal{N}(0, 0.1)$	$(2.23^{+0.22}_{-0.20}) \times 10^{-5}$
$\sigma_{\rm w,K2-5}$	$\mathcal{J}(0.1, 1000)$	$49.88^{+0.78}_{-0.73}$
$\sigma_{\rm GP,K2-5}$	$\mathcal{N}(3.55 \times 10^{-5}, 0.18 \times 10^{-5})$	$(3.55 \pm 0.11) \times 10^{-5}$
$\rho_{\rm GP,K2-5}$	$\mathcal{N}(0.142, 0.019)$	0.137 ± 0.012
$m_{\rm flux,K2-18}$	$\mathcal{N}(0, 0.1)$	$(-0.85^{+0.30}_{-0.3}) \times 10^{-5}$
$\sigma_{\rm w,K2-18}$	$\mathcal{J}(0.1, 1000)$	60.8 ± 1.1
$\sigma_{\rm GP,K2-18}$	$\mathcal{N}(4.67 \times 10^{-5}, 0.28 \times 10^{-5})$	$(4.63^{+0.17}_{-0.16}) \times 10^{-5}$
$\rho_{\rm GP,K2-18}$	$\mathcal{N}(0.094, 0.014)$	0.0944 ± 0.0085
$m_{\rm dilution,K2-5}$ . . .	fixed	1
$m_{\rm dilution,K2-18}$ . . .	fixed	1
a_1 . . . . . . [au]	–	0.1179 ± 0.0004
e_1	–	$0.574^{+0.083}_{-0.090}$
ω_1 . . . . [°]	–	$93.6^{+75.8}_{-263.4}$
i_1 . . . . [°]	–	88.36 ± 0.54
$T_{14,1}$ . . . . . . [h]	–	3.61 ± 0.16
M_1 . . . . . [$M_\oplus$]	–	< 29.8
R_1 . . . . . . [$R_\oplus$]	–	1.216 ± 0.062
ρ_1 . . . . [g cm^{-3}]	–	90.99 ± 20.68
$T_{\rm eq,1}$ . . . . . [K]	–	671.0 ± 13.0
S_1 . . . . . . [$S_\oplus$]	–	33.9 ± 3.0
$\log Z$	–	47499.2 ± 0.5

Notes. *Top*: Fitted parameters. *Bottom*: Derived orbital parameters and physical parameters.

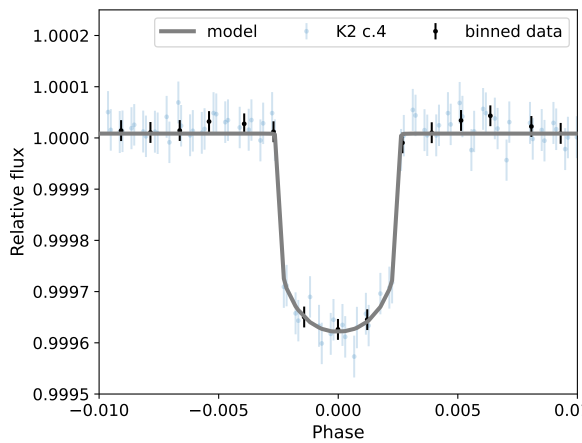

Fig. B.2. Phase-folded K2 data with the median 1*c* model (grey line) for BD+20594 b. The points show the data from K2 campaign 4 (blue) and binned data (black).

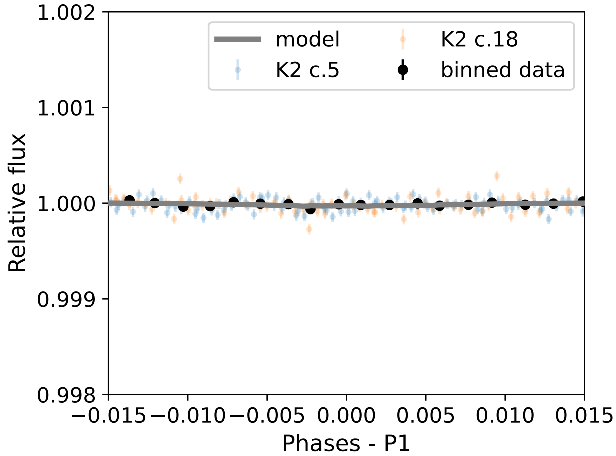

Fig. B.3. Stacked phase-folded K2 data with the median 2*c* model (grey line), for K2-105 b (left) and K2-105 c (right). The points show the data from K2 campaign 5 (blue) and campaign 18 (orange), and binned data (black).

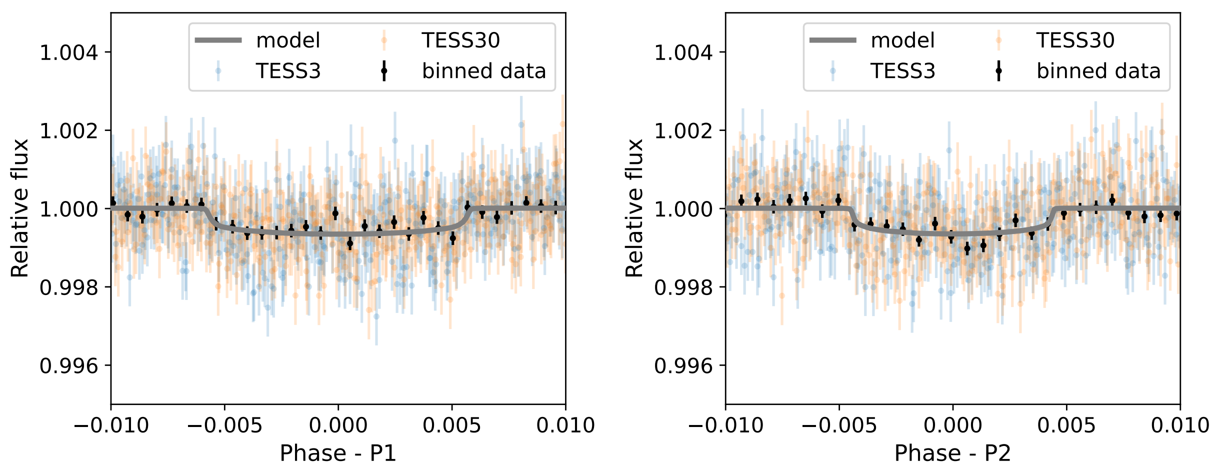

Fig. B.4. Stacked phase-folded PDCSAP TESS data with the median 2*c* model (grey line), for TOI-266 b (left) and TOI-266 c (right). The points show the data from TESS sector 3 (blue) and sector 30 (orange), and binned data (black).

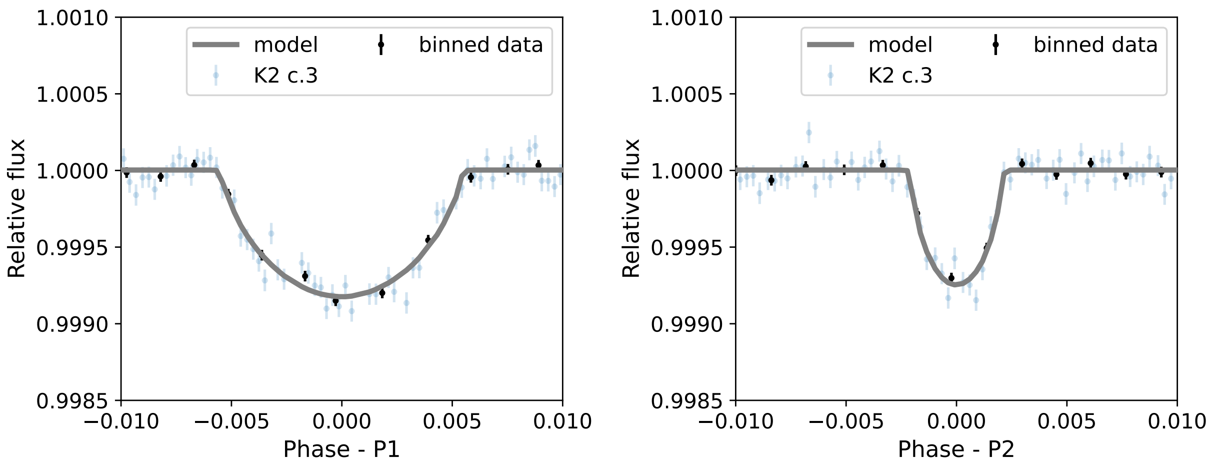

Fig. B.5. Phase-folded K2 data with the median 2*c* model (grey line), for K2-62 b (left) and K2-62 c (right). The points show the data from K2 campaign 3 (blue) and binned data (black).

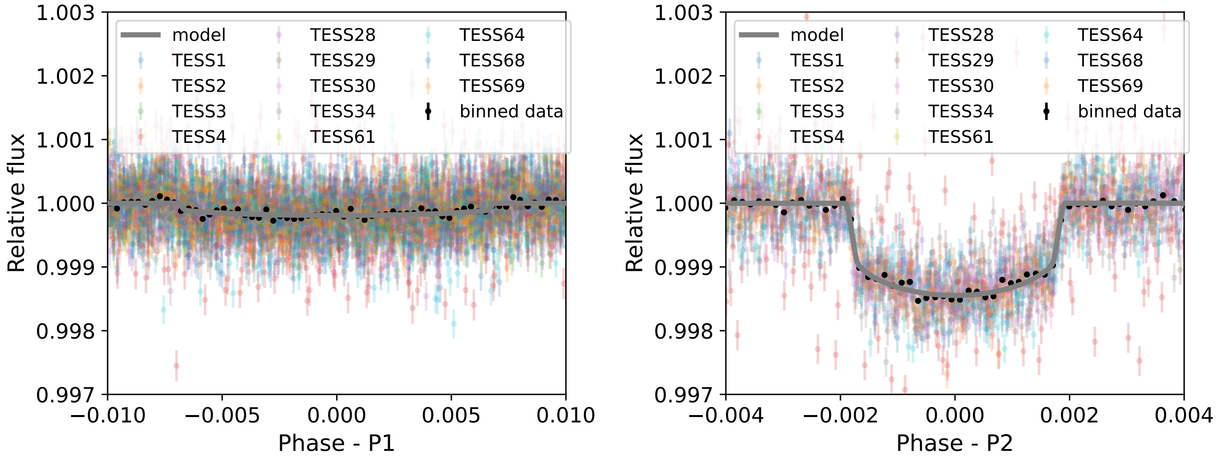

Fig. B.6. Phase-folded TESS data with the median 2*e* model (grey line), for TOI-186 b (left) and TOI-186 c (right). The points show the data from the different TESS sectors (colours) and binned data (black).

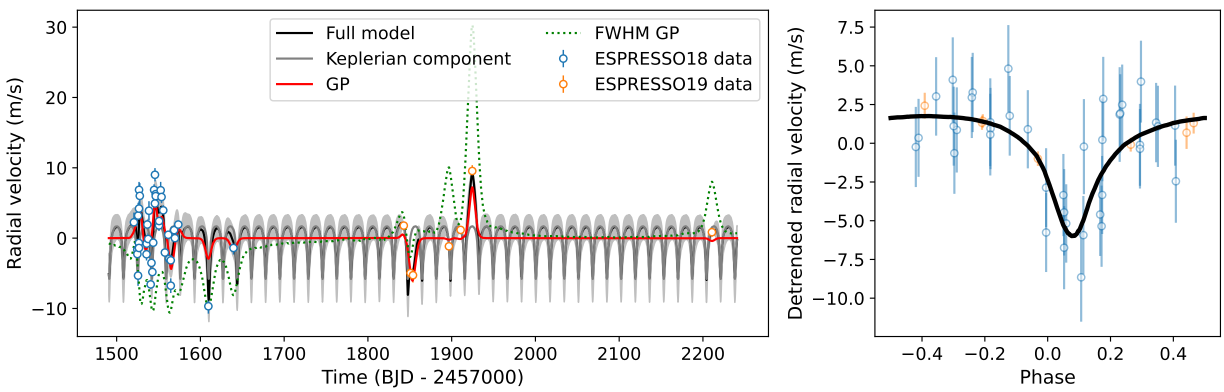

Fig. B.7. Left: ESPRESSO RVs before (blue dots) and after (orange dots) the fibre link replacement and median model (black) for the 1*e_gp* model for K2-184 b. The error bars show the RV errors and jitter added in quadrature. The instrumental systemic velocities have been subtracted. Right: Phase-folded RVs and median Keplerian model.

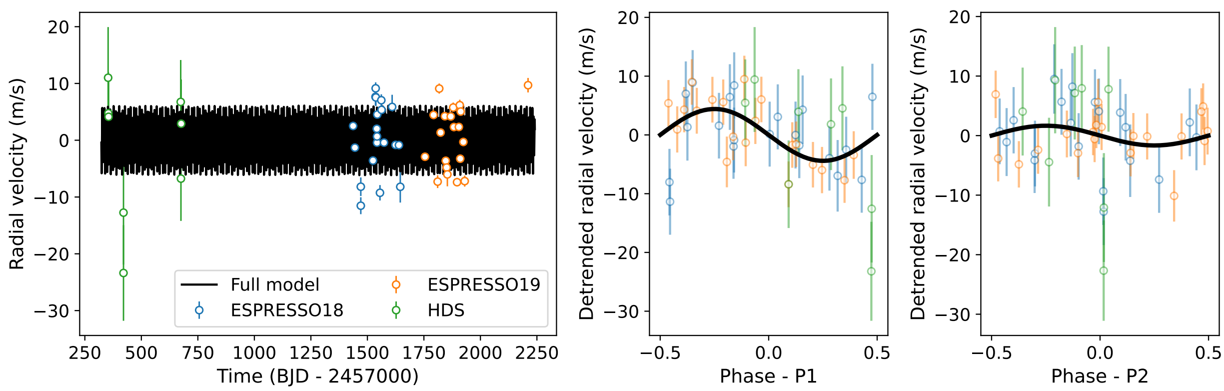

Fig. B.8. Left: ESPRESSO RVs before (blue dots) and after (orange dots) the fibre link replacement, HDS RVs (green dots), and median model (black) for the 2*c* model for K2-105. The error bars show the RV errors and jitter added in quadrature. The instrumental systemic velocities have been subtracted. Centre and right: Phase-folded RVs and median Keplerian model for K2-105 b (centre) and K2-105 c (right).

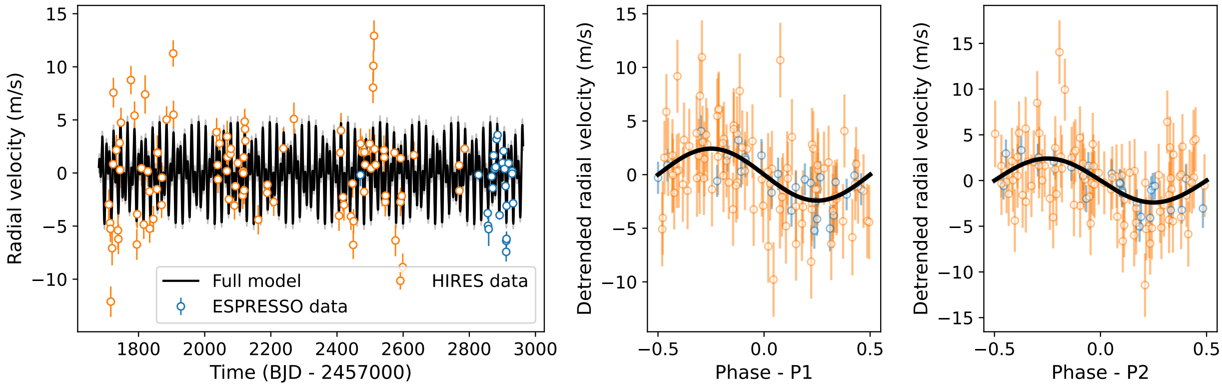

Fig. B.9. Left: ESPRESSO RVs (blue dots), HIRES RVs (orange dots), and median model (black) for the 2*c* model for TOI-266. The error bars show the RV errors and jitter added in quadrature. The instrumental systemic velocities have been subtracted. Centre and right: Phase-folded RVs and median Keplerian model for for TOI-266 b (centre) and TOI-266 c (right).

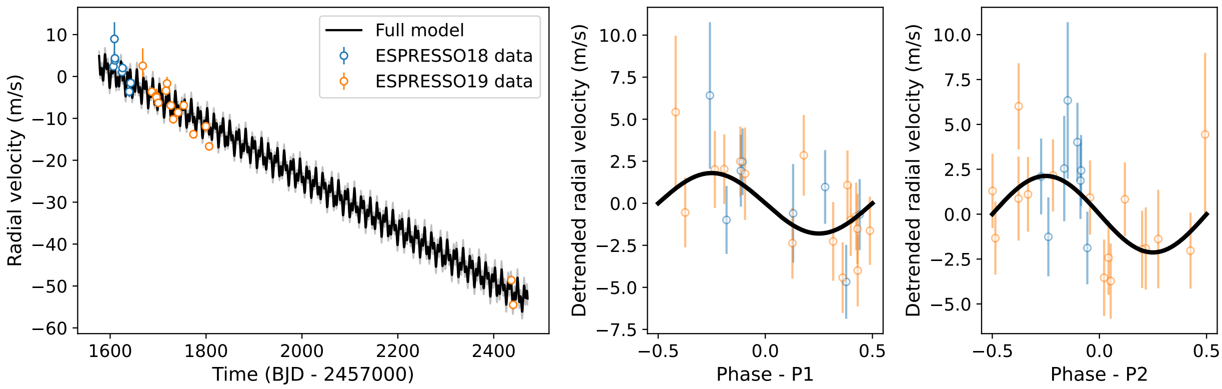

Fig. B.10. Left: ESPRESSO RVs before (blue dots) and after (orange dots) the fibre link replacement, and median model (black) for the 2*c* model for K2-62. The error bars show the RV errors and jitter added in quadrature. The instrumental systemic velocities have been subtracted. Centre and right: Phase-folded RVs and median Keplerian model for K2-62 b (centre) and K2-62 c (right).

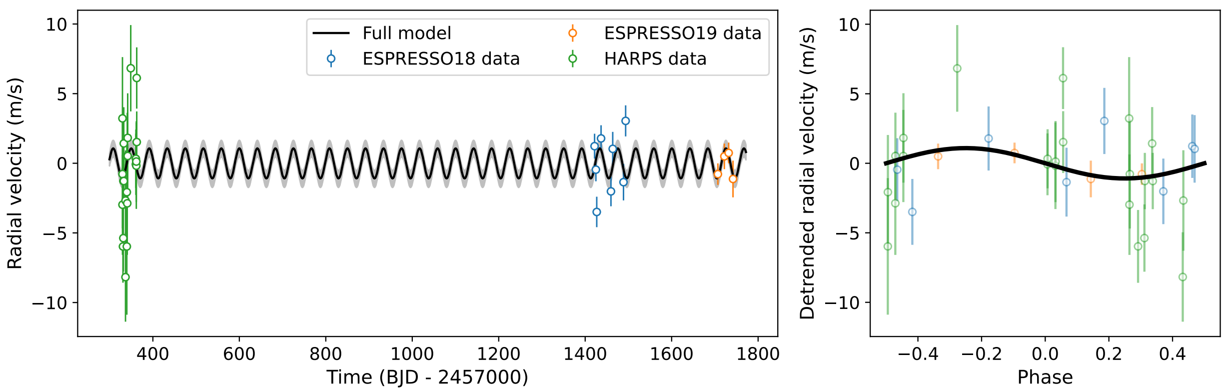

Fig. B.11. Left: ESPRESSO RVs before (blue dots) and after (orange dots) the fibre link replacement, HARPS RVs (green dots), and median model (black) for the 1*c* model for BD+20594 b. The error bars show the RV errors and jitter added in quadrature. The instrumental systemic velocities have been subtracted. Right: Phase-folded RVs and median Keplerian model.

Table B.2. Prior and posterior planetary parameter distributions obtained with `juliet` for K2-105, for the 2*c* model on the full dataset.

Parameter	Prior	Posterior
$\mu_{\mathrm{ESPRESSO18}}$ [m s^{-1}]	$\mathcal{U}(-32546.2, -32525.5)$	-32534.7 ± 1.2
$\sigma_{\mathrm{w,ESPRESSO18}}$ [m s^{-1}]	$\mathcal{J}(0.001, 10)$	$5.42^{+1.01}_{-0.79}$
$\mu_{\mathrm{ESPRESSO19}}$ [m s^{-1}]	$\mathcal{U}(-32540.1, -32523.0)$	-32532.63 ± 0.83
$\sigma_{\mathrm{w,ESPRESSO19}}$ [m s^{-1}]	$\mathcal{J}(0.001, 10)$	$3.77^{+0.79}_{-0.61}$
μ_{Subaru} [m s^{-1}]	$\mathcal{U}(-23.06, 11.33)$	$0.5^{+2.5}_{-2.7}$
$\sigma_{\mathrm{w,Subaru}}$ [m s^{-1}]	$\mathcal{J}(0.001, 10)$	$0.24^{+3.76}_{-0.23}$
P_1 [d]	$\mathcal{N}(5.022, 0.001)$	$5.02173^{+0.00042}_{-0.00065}$
$t_{0,1}$ [BJD]	$\mathcal{N}(2458437.97, 0.01)$	$2458437.97438^{+0.0096}_{-0.0102}$
P_2 [d]	$\mathcal{N}(8.267, 0.001)$	$8.2669721^{+0.0000082}_{-0.0000077}$
$t_{0,2}$ [BJD]	$\mathcal{N}(2457147.99, 0.01)$	$2457147.99182^{+0.00091}_{-0.00093}$
K_1 [m s^{-1}]	$\mathcal{U}(0, 10)$	$4.36^{+0.99}_{-1.04}$
K_2 [m s^{-1}]	$\mathcal{U}(0, 10)$	$1.7^{+1.2}_{-1.0}$
p_1	$\mathcal{U}(0, 0.05)$	$0.0057^{+0.0032}_{-0.0034}$
b_1	$\mathcal{U}(0, 2)$	$0.66^{+0.24}_{-0.39}$
ρ [kg m^{-3}]	$\mathcal{J}(100, 1000)$	$928.9^{+50.7}_{-85.6}$
p_2	$\mathcal{N}(0.0339, 0.1)$	$0.03252^{+0.00069}_{-0.00059}$
b_2	$\mathcal{N}(0.31, 0.1)$	$0.591^{+0.036}_{-0.023}$
$q1_{\mathrm{K2-5,K2-18}}$	$\mathcal{U}(0, 1)$	$0.84^{+0.12}_{-0.16}$
$q2_{\mathrm{K2-5,K2-18}}$	$\mathcal{U}(0, 1)$	$0.26^{+0.14}_{-0.13}$
$m_{\mathrm{flux,K2-5}}$	$\mathcal{N}(0, 0.1)$	$(0.58^{+0.79}_{-0.73}) \times 10^{-5}$
$\sigma_{\mathrm{w,K2-5}}$	$\mathcal{J}(0.1, 1000)$	$120.7^{+4.0}_{-4.1}$
$\sigma_{\mathrm{GP,K2-5}}$	$\mathcal{N}(21.67 \times 10^{-5}, 0.73 \times 10^{-5})$	$(21.00^{+0.47}_{-0.45}) \times 10^{-5}$
$\rho_{\mathrm{GP,K2-5}}$	$\mathcal{N}(0.0439, 0.0041)$	$0.0454^{+0.0026}_{-0.0027}$
$m_{\mathrm{flux,K2-18}}$	$\mathcal{N}(0, 0.1)$	$(-0.3^{+1.4}_{-1.5}) \times 10^{-5}$
$\sigma_{\mathrm{w,K2-18}}$	$\mathcal{J}(0.1, 1000)$	$86.5^{+2.4}_{-2.5}$
$\sigma_{\mathrm{GP,K2-18}}$	$\mathcal{N}(23.5 \times 10^{-5}, 1.0 \times 10^{-5})$	$(23.68^{+0.60}_{-0.62}) \times 10^{-5}$
$\rho_{\mathrm{GP,K2-18}}$	$\mathcal{N}(0.0928, 0.0059)$	$0.0910^{+0.0037}_{-0.0036}$
e_1	fixed	0.0
ω_1 [°]	fixed	90.0
e_2	fixed	0.0
ω_2 [°]	fixed	90.0
$m_{\mathrm{dilution,K2-5}}$	fixed	1
$m_{\mathrm{dilution,K2-18}}$	fixed	1
a_1 [au]	–	0.0559 ± 0.0002
i_1 [°]	–	–
$T_{14,1}$ [h]	–	–
M_1 [$M_\oplus$]	–	11.1 ± 2.7
R_1 [$R_\oplus$]	–	–
ρ_1 [g cm^{-3}]	–	–
$T_{\mathrm{eq},1}$ [K]	–	1037.0 ± 5.0
S_1 [$S_\oplus$]	–	191.6 ± 4.0
a_2 [au]	–	0.078 ± 0.0002
i_2 [°]	–	88.21 ± 0.11
$T_{14,2}$ [h]	–	2.83 ± 0.09
M_2 [$M_\oplus$]	–	< 15.5
R_2 [$R_\oplus$]	–	3.145 ± 0.073
ρ_2 [g cm^{-3}]	–	2.73 ± 0.64
$T_{\mathrm{eq},2}$ [K]	–	878.0 ± 5.0
S_2 [$S_\oplus$]	–	98.5 ± 2.0
log Z	–	41266.4 ± 0.5

Notes. *Top*: Fitted parameters. *Bottom*: derived orbital parameters and physical parameters.

Table B.3. Prior and posterior planetary parameter distributions obtained with `juliet` for TOI-266, for the 2*c* model with all data.

Parameter	Prior	Posterior
μ_{ESPRESSO} [m s^{-1}]	$\mathcal{U}(41398.7, 41409.7)$	41406.16 ± 0.31
$\sigma_{\mathrm{w,ESPRESSO}}$ [m s^{-1}]	$\mathcal{J}(0.001, 10)$	$1.42^{+0.26}_{-0.20}$
μ_{HIRES} [m s^{-1}]	$\mathcal{U}(-13.53, 11.50)$	$-1.42^{+0.36}_{-0.35}$
$\sigma_{\mathrm{w,HIRES}}$ [m s^{-1}]	$\mathcal{J}(0.001, 10)$	$3.17^{+0.28}_{-0.25}$
P_1 [d]	$\mathcal{N}(10.751, 0.001)$	$10.751014^{+0.000053}_{-0.000058}$
$t_{0,1}$ [BJD]	$\mathcal{N}(2458393.09, 0.01)$	$2458393.0855^{+0.0031}_{-0.0026}$
K_1 [m s^{-1}]	$\mathcal{U}(0.0, 10)$	2.42 ± 0.30
ρ [kg m^{-3}]	$\mathcal{J}(100, 10000)$	$1901.5^{+357.3}_{-309.7}$
p_1	$\mathcal{N}(0.0242, 0.1)$	0.0246 ± 0.0011
b_1	$\mathcal{N}(0.52, 0.1)$	$0.583^{+0.065}_{-0.069}$
P_2 [d]	$\mathcal{N}(19.606, 0.001)$	19.60550 ± 0.00018
$t_{0,2}$ [BJD]	$\mathcal{N}(2458398.29, 0.01)$	$2458398.2917^{+0.0057}_{-0.0048}$
K_2 [m s^{-1}]	$\mathcal{U}(0, 10)$	$2.41^{+0.33}_{-0.32}$
p_2	$\mathcal{N}(0.0241, 0.1)$	$0.0237459057^{+0.0012}_{-0.0013}$
b_2	$\mathcal{N}(0.4, 0.1)$	$0.354^{+0.081}_{-0.090}$
$q_{1,\mathrm{TESS}}$	$\mathcal{U}(0.0, 1.0)$	$0.34^{+0.37}_{-0.22}$
$q_{2,\mathrm{TESS}}$	$\mathcal{U}(0.0, 1.0)$	$0.39^{+0.35}_{-0.27}$
$m_{\mathrm{flux,TESS3}}$	$\mathcal{N}(0.0, 0.1)$	$(-1.6^{+3.4}_{-3.1}) \times 10^{-5}$
$\sigma_{\mathrm{w,TESS3}}$	$\mathcal{J}(0.1, 1000.0)$	$1.6^{+8.7}_{-1.3}$
$\sigma_{\mathrm{GP,TESS3}}$	$\mathcal{N}(1.6 \times 10^{-5}, 4.1 \times 10^{-5})$	$(3.4^{+2.8}_{-2.2}) \times 10^{-5}$
$\rho_{\mathrm{GP,TESS3}}$	$\mathcal{N}(6.1, 287.5)$	$222.9^{+199.4}_{-134.8}$
$m_{\mathrm{flux,TESS30}}$	$\mathcal{N}(0, 0.1)$	$(-1.0 \pm -1.3) \times 10^{-5}$
$\sigma_{\mathrm{w,TESS30}}$	$\mathcal{J}(0.1, 1000)$	$144.9^{+22.0}_{-29.3}$
$\sigma_{\mathrm{GP,TESS30}}$	$\mathcal{N}(10.4 \times 10^{-5}, 1.1 \times 10^{-5})$	$(10.25^{+0.76}_{-0.74}) \times 10^{-5}$
$\rho_{\mathrm{GP,TESS30}}$	$\mathcal{N}(0.112, 0.036)$	$0.114^{+0.022}_{-0.019}$
e_1	fixed	0
ω_1 [°]	fixed	90
e_2	fixed	0
ω_2 [°]	fixed	90
a_1 [au]	–	0.0899 ± 0.0001
i_1 [°]	–	88.35 ± 0.2
$T_{14,1}$ [h]	–	3.44 ± 0.2
M_1 [$M_\oplus$]	–	7.39 ± 0.92
R_1 [$R_\oplus$]	–	2.57 ± 0.12
ρ_1 [g cm^{-3}]	–	2.39 ± 0.44
$T_{\mathrm{eq},1}$ [K]	–	884.0 ± 3.0
S_1 [$S_\oplus$]	–	101.6 ± 1.0
a_2 [au]	–	0.1341 ± 0.0002
i_2 [°]	–	89.33 ± 0.17
$T_{14,2}$ [h]	–	4.79 ± 0.17
M_2 [$M_\oplus$]	–	9.0 ± 1.2
R_2 [$R_\oplus$]	–	2.48 ± 0.14
ρ_2 [g cm^{-3}]	–	3.26 ± 0.7
$T_{\mathrm{eq},2}$ [K]	–	723.0 ± 3.0
S_2 [$S_\oplus$]	–	45.6 ± 1.0
log Z	–	165320.3 ± 0.5

Notes. *Top*: Fitted parameters. *Bottom*: derived orbital parameters and physical parameters.

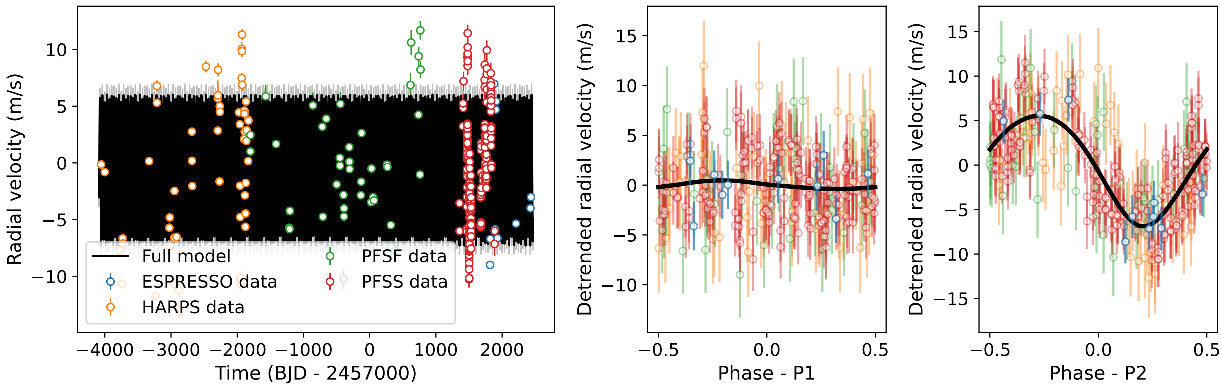

Fig. B.12. Left: ESPRESSO RVs (blue dots), HARPS RVs (orange dots), PFS RVs before (green dots) and after (red dots) the 2018 detector and slit change, and median model (black) for the 2*e* model for TOI-186. The error bars show the RV errors and jitter added in quadrature. The instrumental systemic velocities have been subtracted. Centre and right: Phase-folded RVs and median Keplerian model for TOI-186 b (centre) and TOI-186 c (right).

Table B.4. Prior and posterior planetary parameter distributions obtained with `juliet` for K2-62, for the 2*c* model.

Parameter	Prior	Posterior
$\mu_{\rm ESPRESSO18}$ [m s^{-1}]	$\mathcal{U}(4360.0, 4372.6)$	$4363.7^{+2.3}_{-2.4}$
$\sigma_{\rm w,ESPRESSO18}$ [m s^{-1}]	$\mathcal{J}(0.001, 10)$	1.8 ± 1.0
$\mu_{\rm ESPRESSO19}$ [m s^{-1}]	$\mathcal{U}(4305.4, 4362.4)$	$4359.9^{+1.8}_{-2.5}$
$\sigma_{\rm w,ESPRESSO19}$ [m s^{-1}]	$\mathcal{J}(0.001, 10)$	$1.81^{+0.65}_{-0.50}$
P_1 .... [d]	$\mathcal{N}(6.672, 0.001)$	$6.67188^{+0.00024}_{-0.00026}$
$t_{0,1}$ ..... [BJD]	$\mathcal{N}(2456982.69, 0.01)$	$2456982.6856115987^{+0.0014}_{-0.0013}$
K_1 .... [m s^{-1}]	$\mathcal{U}(0, 10)$	$1.77^{+0.69}_{-0.61}$
ρ .... [kg m^{-3}]	$\mathcal{J}(100, 10000)$	$7824.4^{+1458.1}_{-2736.5}$
p_1	$\mathcal{N}(0.027, 0.1)$	$0.0243^{+0.0027}_{-0.0016}$
b_1	$\mathcal{U}(0, 1)$	$0.45^{+0.20}_{-0.16}$
P_2 .... [d]	$\mathcal{N}(16.197, 0.001)$	16.19752 ± 0.00081
$t_{0,2}$ ..... [BJD]	$\mathcal{N}(2456991.54, 0.01)$	2456991.5437 ± 0.0015
K_2 .... [m s^{-1}]	$\mathcal{U}(0, 10)$	$2.19^{+0.89}_{-0.92}$
p_2	$\mathcal{N}(0.027, 0.1)$	$0.0299^{+0.0022}_{-0.0018}$
b_2	$\mathcal{U}(0, 1)$	$0.795^{+0.063}_{-0.042}$
$q_{1,K2}$	$\mathcal{U}(0, 1)$	$0.87^{+0.09}_{-0.13}$
$q_{2,K2}$	$\mathcal{U}(0, 1)$	$0.78^{+0.14}_{-0.21}$
$rv_{\rm intercept}$ .. [m s^{-1}]	$\mathcal{U}(-100, 100)$	$10.1^{+2.5}_{-2.1}$
$rv_{\rm slope}$ ... [m s^{-1}]	$\mathcal{U}(-100, 100)$	-0.0627 ± 0.0023
$m_{\rm flux,K2-3}$	$\mathcal{N}(0, 0.1)$	$(-2.8^{+4.2}_{-0.000004.0}) \times 10^{-6}$
$\sigma_{\rm w,K2-3}$	$\mathcal{J}(0.1, 1000)$	$65.8^{+2.0}_{-1.9}$
$\sigma_{\rm GP,K2-3}$	$\mathcal{N}(5.6 \times 10^{-5}, 0.3 \times 10^{-5})$	$(5.55^{+0.20}_{-0.21}) \times 10^{-5}$
$\rho_{\rm GP,K2-3}$	$\mathcal{N}(0.161, 0.023)$	$0.16^{+0.016}_{-0.015}$
e_1	fixed	0
ω_1 .... [°]	fixed	90
e_2	fixed	0
ω_2 .... [°]	fixed	90
fixed	1	
a_1 ...... [au]	–	0.0606 ± 0.0002
i_1 .... [°]	–	88.68 ± 0.59
$T_{14,1}$ ...... [h]	–	2.4 ± 0.26
M_1 ..... [$M_\oplus$]	–	< 8.6
R_1 ...... [$R_\oplus$]	–	1.77 ± 0.20
ρ_1 .... [g cm^{-3}]	–	8.63 ± 3.27
$T_{\rm eq,1}$ ..... [K]	–	745.0 ± 3.0
S_1 ...... [$S_\oplus$]	–	51.4 ± 1.0
a_2 ...... [au]	–	0.1095 ± 0.0003
i_2 .... [°]	–	88.72 ± 0.1
$T_{14,2}$ ...... [h]	–	2.31 ± 0.25
M_2 ..... [$M_\oplus$]	–	< 14.7
R_2 ...... [$R_\oplus$]	–	2.17 ± 0.16
ρ_2 .... [g cm^{-3}]	–	7.88 ± 2.29
$T_{\rm eq,2}$ ..... [K]	–	554.0 ± 2.0
S_2 ...... [$S_\oplus$]	–	15.8 ± 0.0
log Z	–	24602.0 ± 0.6

Notes. *Top*: Fitted parameters. *Bottom*: Derived orbital parameters and physical parameters.

Table B.5. Prior and posterior planetary parameter distributions obtained with `juliet` for BD+20954, for the 1*c* model on the joint dataset.

Parameter	Prior	Posterior
$\mu_{\rm ESPRESSO18}$ [m s^{-1}]	$\mathcal{U}(-20494.4, -20489.6)$	$-20490.87^{+0.66}_{-0.71}$
$\sigma_{\rm w,ESPRESSO18}$ [m s^{-1}]	$\mathcal{J}(0.001, 10)$	$2.10^{+0.86}_{-0.64}$
$\mu_{\rm ESPRESSO19}$ [m s^{-1}]	$\mathcal{U}(-20496.0, -20494.1)$	$-20494.89^{+0.40}_{-0.46}$
$\sigma_{\rm w,ESPRESSO19}$ [m s^{-1}]	$\mathcal{J}(0.001, 10)$	$0.023^{+0.223}_{-0.020}$
$\mu_{\rm HARPS}$ ... [m s^{-1}]	$\mathcal{U}(-20345.3, -20330.3)$	$-20337.12^{+0.59}_{-0.65}$
$\sigma_{\rm w,HARPS}$ .. [m s^{-1}]	$\mathcal{J}(0.001, 10)$	$0.31^{+1.51}_{-0.30}$
P_1 .... [d]	$\mathcal{N}(41.686, 0.001)$	$41.68547^{+0.00097}_{-0.00094}$
$t_{0,1}$ ..... [BJD]	$\mathcal{N}(2457151.90, 0.01)$	$2457151.9014^{+0.0034}_{-0.0035}$
K_1 .... [m s^{-1}]	$\mathcal{U}(0, 10)$	$1.08^{+0.46}_{-0.44}$
ρ .... [kg m^{-3}]	$\mathcal{J}(100, 10000)$	$1758.5^{+905.8}_{-1201.6}$
p_1	$\mathcal{U}(0.005, 0.05)$	$0.0188^{+0.0017}_{-0.0009}$
b_1	$\mathcal{U}(0, 1)$	$0.50^{+0.31}_{-0.38}$
$q_{1,K2}$	$\mathcal{U}(0, 1)$	$0.34^{+0.28}_{-0.22}$
$q_{2,K2}$	$\mathcal{U}(0, 1)$	$0.37^{+0.35}_{-0.25}$
$m_{\rm flux,K2-4}$	$\mathcal{N}(0, 0.1)$	$(-0.86^{+0.18}_{-0.20}) \times 10^{-5}$
$\sigma_{\rm w,K2-4}$	$\mathcal{J}(0.1, 1000)$	$0.97^{+4.28}_{-0.75}$
$\sigma_{\rm GP,K2-4}$	$\mathcal{N}(7.31 \times 10^{-5}, 0.14 \times 10^{-5})$	$(7.341^{+0.090}_{-0.00000.089}) \times 10^{-5}$
$\rho_{\rm GP,K2-4}$	$\mathcal{N}(0.01561, 0.00068)$	$0.01575^{+0.00044}_{-0.00046}$
e_1	fixed	0
ω_1 .... [°]	fixed	90
$m_{\rm dilution,K2-4}$ ...	fixed	1
a_1 ...... [au]	–	0.2226 ± 0.0002
i_1 .... [°]	–	89.35 ± 0.49
$T_{14,1}$ ...... [h]	–	6.42 ± 1.55
M_1 ..... [$M_\oplus$]	–	< 12.0
R_1 ...... [$R_\oplus$]	–	2.23 ± 0.20
ρ_1 .... [g cm^{-3}]	–	5.91 ± 1.95
$T_{\rm eq,1}$ ..... [K]	–	613.0 ± 4.0
S_1 ...... [$S_\oplus$]	–	23.9 ± 1.0
log Z	–	25990.0 ± 0.4

Notes. *Top*: Fitted parameters. *Bottom*: Derived orbital parameters and physical parameters.

Table B.6. Prior and posterior planetary parameter distributions obtained with `juliet` for TOI-186, for the 2*e* model on the joint dataset.

Parameter	Prior	Posterior
μ_{ESPRESSO} [m s^{-1}]	$\mathcal{U}(59595.4, 59611.4)$	$59604.41^{+0.76}_{-0.73}$
$\sigma_{\mathrm{w,ESPRESSO}}$ [m s^{-1}]	$\mathcal{J}(0.001, 10)$	$2.43^{+0.74}_{-0.50}$
μ_{HARPS} . . [m s^{-1}]	$\mathcal{U}(-13.2, 11.2)$	$-0.12^{+0.57}_{-0.56}$
$\sigma_{\mathrm{w,HARPS}}$. [m s^{-1}]	$\mathcal{J}(0.001, 10)$	$4.44^{+0.46}_{-0.41}$
μ_{PFSF} . . . [m s^{-1}]	$\mathcal{U}(-10.1, 11.8)$	0.10 ± 0.68
$\sigma_{\mathrm{w,PFSF}}$ . . [m s^{-1}]	$\mathcal{J}(0.001, 10)$	$4.24^{+0.53}_{-0.42}$
μ_{PFSS} . . . [m s^{-1}]	$\mathcal{U}(-9.7, 12.0)$	$0.51^{+0.25}_{-0.24}$
$\sigma_{\mathrm{w,PFSS}}$ . . [m s^{-1}]	$\mathcal{J}(0.001, 10)$	$3.01^{+0.18}_{-0.17}$
P_1 . . . . . . [d]	$\mathcal{N}(7.790, 0.001)$	$7.789787^{+0.000018}_{-0.000013}$
$t_{0,1}$ . . . . [BJD]	$\mathcal{N}(2458371.23, 0.01)$	$2458371.2286^{+0.0016}_{-0.0013}$
$\sqrt{e}\sin\omega_1$	$\mathcal{U}(-1, 1)$	$-0.37^{+0.17}_{-0.12}$
$\sqrt{e}\cos\omega_1$	$\mathcal{U}(-1, 1)$	$0.29^{+0.27}_{-0.34}$
e_1	–	$0.25^{+0.20}_{-0.13}$
ω_1 . . . . . . [°]	–	$-49.0^{+20.3}_{-47.3}$
K_1 . . . . [m s^{-1}]	$\mathcal{U}(0, 10)$	$0.57^{+0.32}_{-0.29}$
ρ . . . . [kg m^{-3}]	$\mathcal{J}(100, 10000)$	$4922.8^{+1324.6}_{-1072.6}$
p_1	$\mathcal{N}(0.012, 0.1)$	$0.01272^{+0.00049}_{-0.00047}$
b_1	$\mathcal{N}(0.42, 0.1)$	$0.401^{+0.087}_{-0.096}$
P_2 . . . . . . [d]	$\mathcal{N}(35.613, 0.001)$	35.613442 ± 0.000016
$t_{0,2}$ . . . . [BJD]	$\mathcal{N}(2458385.93, 0.01)$	$2458385.92562^{+0.00054}_{-0.00052}$
$\sqrt{e}\sin\omega_2$	$\mathcal{U}(-1, 1)$	0.08 ± 0.14
$\sqrt{e}\cos\omega_2$	$\mathcal{U}(-1, 1)$	$-0.319^{+0.050}_{-0.034}$
e_2	–	0.122 ± 0.022
ω_2 . . . . . . [°]	–	$146.0^{+23.4}_{-313.7}$
K_2 . . . . [m s^{-1}]	$\mathcal{U}(0, 10)$	$6.24^{+0.30}_{-0.31}$
p_2	$\mathcal{N}(0.024, 0.1)$	$0.03630^{+0.00078}_{-0.00072}$
b_2	$\mathcal{N}(0.59, 0.1)$	$0.584^{+0.066}_{-0.077}$
$q_{1,\mathrm{TESS}}$	$\mathcal{U}(0, 1)$	$0.29^{+0.11}_{-0.07}$
$q_{2,\mathrm{TESS}}$	$\mathcal{U}(0, 1)$	$0.62^{+0.23}_{-0.27}$
a_1 . . . . . [au]	–	0.0691 ± 0.0002
i_1 . . . . . . [°]	–	89.05 ± 0.29
$T_{14,1}$ . . . . . [h]	–	2.64 ± 0.12
M_1 . . . . [$M_\oplus$]	–	< 3.83
R_1 . . . . . [$R_\oplus$]	–	0.984 ± 0.038
ρ_1 . . . [g cm^{-3}]	–	22.08 ± 5.29
$T_{\mathrm{eq},1}$ . . . . . [K]	–	728.0 ± 10.0
S_1 . . . . . [$S_\oplus$]	–	46.5 ± 3.0
a_2 . . . . . [au]	–	0.1904 ± 0.0005
i_2 . . . . . . [°]	–	89.38 ± 0.33
$T_{14,2}$ . . . . . [h]	–	4.05 ± 0.26
M_2 . . . . [$M_\oplus$]	–	25.9 ± 1.3
R_2 . . . . . [$R_\oplus$]	–	2.809 ± 0.062
ρ_2 . . . [g cm^{-3}]	–	6.43 ± 0.53
$T_{\mathrm{eq},2}$ . . . . . [K]	–	436.0 ± 2.0
S_2 . . . . . [$S_\oplus$]	–	6.0 ± 0.0
$\log Z$	–	61324.3 ± 0.6

Notes. *Top*: Fitted parameters. *Bottom*: derived orbital parameters and physical parameters.

Appendix C: ExoMDN model output plots

In this section, we present the results of the ExoMDN modelling described in section 4.1.

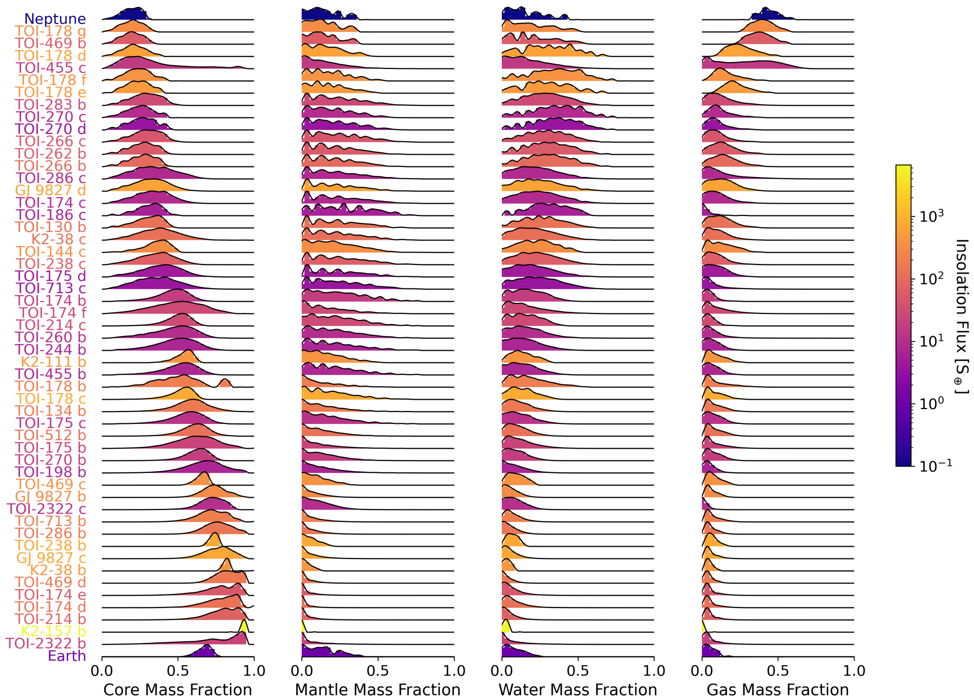

Fig. C.1. Normalised histograms of the core, mantle, water, and gas mass fraction posteriors obtained with ExoMDN for the WG3 sample. The planets are ordered by core mass fraction and labelled. We include the Earth and Neptune at the bottom and top, respectively, as comparison points.

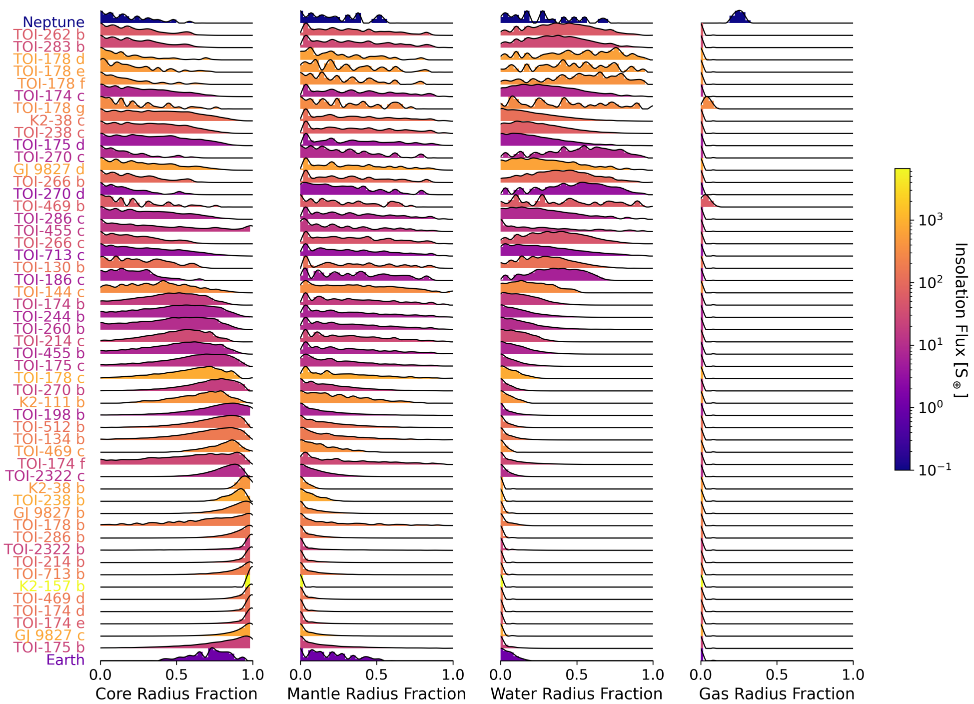

Fig. C.2. Normalised histograms of the core, mantle, water, and gas radius fraction posteriors obtained with ExoMDN for the WG3 sample. The planets are ordered by core radius fraction. We include the Earth and Neptune at the bottom and top, respectively, as comparison points.